A SEMI-ANALYTICAL VARIABLE PROPERTY DROPLET COMBUSTION MODEL

by

John Sisti

September 2013

A thesis submitted to the

Faculty of the Graduate School of

the University at Buffalo, State University of New York

in partial fulfilment of the requirements for the

degree of

Master of Science

Department of Mechanical and Aerospace Engineering

UMI Number: 1546974

All rights reserved

INFORMATION TO ALL USERS
The quality of this reproduction is dependent upon the quality of the copy submitted.

In the unlikely event that the author did not send a complete manuscript
and there are missing pages, these will be noted. Also, if material had to be removed,
a note will indicate the deletion.

UMI 1546974

Published by ProQuest LLC (2013). Copyright in the Dissertation held by the Author.

Microform Edition © ProQuest LLC.
All rights reserved. This work is protected against
unauthorized copying under Title 17, United States Code

ProQuest LLC.
789 East Eisenhower Parkway
P.O. Box 1346
Ann Arbor, MI 48106 - 1346

Acknowledgments

I would first like to thank my advisor, Dr. Paul E. DesJardin, for his continued support, guidance, knowledge, and enthusiasm with this work. I would also like to thank the members of my committee, Dr. James D. Felske and Dr. Matthew Ringuette, both of which have contributed to my development as a student in the research environment. I would also like to show my appreciation to my colleagues, Dr. Matthew McGurn, Brian Bojko, and Hafez Asgharzadeh, for their insight, particularly when they paused their own work to give it.

Support for this work has been provided by NAVAIR through the STTR phase II program under contract N68335-10-C-0418.

Table of Contents

Acknowledgments ii

List of Tables v

List of Figures vi

Nomenclature viii

Abstract ix

Chapter 1
Introduction 1

Chapter 2
Quiesent Quasi-steady Burning 5
2.1 Model Formulation 5
2.2 Numerical Implementation 10
2.3 Evaporating Droplet 15
2.4 Results 15

Chapter 3
Extension to Convective Transient Burning 32
3.1 Formulation 32
3.1.1 Convection Extension 33
3.1.2 Transient Extension 35
3.2 Results 37

Chapter 4
Conclusions 42

Appendix A
Solution of Eigenvalue Problem **44**

Bibliography **49**

List of Tables

2.1 Burning rates, stand-off ratios, flame and surface temperatures for selected fuels at selected states. The two-zone calculation is denoted by parentheses ( ). 20

List of Figures

2.1 Sketch of multizone droplet description. 21
2.2 Illustration of mesh adaptivity showing (a) shell positions and (b) r_{in}^{**} verses η_{in} for $\Delta T_{max} = 100\,K$. 22
2.3 Error in K, r_f^* and T_f verses ΔT_{max} and N for (a) n-heptane, (b) ethanol and (c) methanol. For all cases $T_\infty = 298\,K$, $P_\infty = 1\,ATM$ and $Y_{O,\infty} = 0.23$. 23
2.4 n-Heptane droplet flame structure showing (a) T, Y_i and (b) Le, Λ_P, C_P, k and Γ. For this case, $\Delta T_{max} = 1\,K$, $T_\infty = 298\,K$, $P_\infty = 1\,ATM$ and $Y_{O,\infty} = 0.23$. 24
2.5 Ethanol droplet flame structure showing (a) T, Y_i and (b) Le, Λ_P, C_P, k and Γ. For this case, $\Delta T_{max} = 1\,K$, $T_\infty = 298\,K$, $P_\infty = 1\,ATM$ and $Y_{O,\infty} = 0.23$. 25
2.6 Methanol droplet flame structure showing (a) T, Y_i and (b) Le, Λ_P, C_P, k and Γ. For this case, $\Delta T_{max} = 1\,K$, $T_\infty = 298\,K$, $P_\infty = 1\,ATM$ and $Y_{O,\infty} = 0.23$. 26
2.7 n-Heptane droplet flame structure showing T, Y_F and Y_O [1, 2]. For this case, $\Delta T_{max} = 1\,K$, $T_\infty = 298\,K$, $P_\infty = 1\,ATM$ and $Y_{O,\infty} = 0.23$. 27
2.8 n-heptane (a) burn rate and (b) flame stand-off ratio verses $Y_{O,\infty}$ [1, 3, 4]. For all cases $\Delta T_{max} = 1\,K$, $T_\infty = 298\,K$ and $P_\infty = 1\,ATM$. . 28
2.9 Ethanol (a) burn rate and (b) flame stand-off ratio verses $Y_{O,\infty}$ [3, 4, 5]. For all cases $\Delta T_{max} = 1\,K$, $T_\infty = 298\,K$ and $P_\infty = 1\,ATM$. . 29
2.10 Methanol (a) burn rate and (b) flame stand-off ratio verses $Y_{O,\infty}$ [6, 7, 8, 9, 10, 11]. For all cases $\Delta T_{max} = 1\,K$, $T_\infty = 298\,K$ and $P_\infty = 1\,ATM$. 30
2.11 Methanol burn rate verses $X_{CO_2,\infty}$ [7]. For all cases, $\Delta T_{max} = 1\,K$, $T_\infty = 298\,K$, $P_\infty = 1\,ATM$ and $X_{O,\infty} = 0.21$. 31

3.1 Isolated burning methanol droplet in varying CO_2 environments showing simulated and experimental (a) diameter squared vs. time normalized by the initial diameter squared and (b) stand-off ratio vs. time. 39

3.2 Error for mass, momentum, and energy in comparison to ODE solution through time vs. time-step size determined by the factor $\frac{\Delta t}{\tau}$ at various Reynolds numbers. 40
3.3 Time history for diameter squared. 40
3.4 Time history for velocity. 41
3.5 Time history for temperature. 41

A.1 Flow chart of algorithm for solution of droplet eigenvalue problem. 48

Nomenclature

B_q	Thermal transport number $[-]$
C_P	Mass weighted specific heat $[Jkg^{-1}K^{-1}]$
D	Diffusivity coefficient $[m^2s^{-1}]$
K	Gasification rate $[mm^2s^{-1}]$
h	Enthalpy $[Jkg^{-1}]$
Δh_C	Heat of combustion $[Jkg^{-1}]$
k	Thermal conductivity $[Wm^{-1}K^{-1}]$
L	Fuel-Oxidizer concentration factor $[-]$
L'_{vap}	Effective latent heat of vaporization $[Jkg^{-1}]$
Le	Lewis number $[-]$
m	Mass $[kg]$
$\dot{m}$	Mass flow-rate $[kgs^{-1}]$
N	Number of zones $[-]$
$\dot{q}''$	Heat flux $[Wkg^{-1}m^{-2}]$
$\dot{Q}$	Heat flow-rate $[W]$
r	Radius $[m]$
r^*	Surface normalized radius $[-]$
r^{**}	Flame-surface or far-field-flame normalized radius $[-]$
T	Temperature $[K]$
ΔT	Initial temperature difference between shells $[K]$
X	Mole fraction $[-]$
Y	Mass fraction $[-]$

Greek

Γ	ρD $[kgm^{-1}s^{-1}]$
ϵ_i	$\frac{\dot{m}_i}{\dot{m}}$ $[-]$
η	Temperature-space $[-]$
Λ_P	Mass-flow weighted specific heat $[Jkg^{-1}K^{-1}]$
ν_i	Stoichiometric ratio of mass of i^{th} species $[-]$
ρ	Density $[kgm^{-3}]$
ϕ	$-\frac{\dot{m}}{2\pi r_s}$ $[kgm^{-1}s^{-1}]$

Subscripts/Superscripts

ad	Adiabadic
f	Flame shell
F	Fuel species
i	Species
in	Inner region
k	Shell number
l	Liquid property
m	Mixture
max	Maximum
out	Outer region
O	Oxidizer species
p	Product species
s	Surface shell
∞	Far-field shell

Abstract

A multizone droplet burn model is developed to account for changes in the thermal and transport properties as a function of droplet radius. The formulation is semi-analytical - allowing for accurate and computationally efficient estimates of flame structure and burn rates. Zonal thermal and transport properties are computed using the Cantera software and pre-tabulated for rapid evaluation during run-time. Model predictions are compared to experimental measurements of burning *n*-heptane, ethanol and methanol droplets. An adaptive zone refinement algorithm is developed that minimizes the number of zones required to provide accurate estimates of burn time without excess zones. A sensitivity study of burn rate and flame stand-off with far-field oxygen concentration is conducted with comparisons to experimental data. Overall agreement to data is encouraging with errors typically less than 20% for predictions of burn rates, stand-off ratio and flame temperature for the fuels considered. The quiescent quasi-steady solution is extended to a convective transient solution without the need to solve an eigenvalue solution in time. The time history of the burning droplets show good comparison with experimental data. To further decrease computational cost, the source terms for the transient solution are linearized for an explicit time marching solution. An error convergence study was performed to show a time-step independent solution exists at a reasonable Δt.

Chapter 1

Introduction

The topic of droplet combustion has a rich history. Reviews and texts on droplet combustion include those of Faeth [12, 13], Sirignano [14, 15], Williams [16, 17], Law [18], Kuo [19], Turns [20], Glassman [21]. Early theories of droplet burning came from Spaulding [22], Godsave [23] and Lorell *et al.* [24, 25] and were based on either single or two-zone descriptions with constant properties within each zone. While these early theories are elegant and relatively simple to formulate, they are also known to greatly over-predict the flame radius and under-predict burn times [18, 26]. Since flame radii and burn rates are measurable in droplet experiments, it is important to have a droplet burn model that is sufficiently accurate to predict these quantities. The major source of the modeling assumption error leading to the exaggerated flame radius is the relative independence of thermal and transport properties to flame radius, stemming from changes in composition and temperature that are not accounted for in the two-zone model.

Many enhancements to these early theories have improved the description of property variation either through improved analytics [27, 28] or direct numerical integration [2].

For the current effort, it is highly desirable for the droplet model be computationally efficient since its intended use is in a subgrid scale (SGS) model for large eddy simulations of turbulent reacting, multiphase flows in a dilute limit [29, 30]. Current models for droplet burning usually fall into two categories. The first are detailed numerical integration where the governing equations are numerically discretized, linearized and solved, *e.g.* Refs. [1, 2, 31, 32, 33]. These computations are often demanding since sufficient resolution is required to approximate the gradients of temperature and composition. While these models are valuable for understanding quasi-steady burning behavior of isolated droplets, they contain far too many degrees of freedom for incorporation into a larger spray calculation for which millions of droplets (or groups of droplets) are transported.

The second category of models are entirely analytical. This class of model relies on layers of approximations to obtain a closed form solution. This category includes the model developed by Law and Law [28] to account for variable transport properties. In their model, the transport properties are first assumed separable in terms of their temperature and composition dependence. The dependence of each function is assumed to follow a particular form (often linear).

The functional form of the mixing rules for transport properties also has to be chosen with care to allow for a tractable result. At the end of the analysis, numerical integration is still required for the most general description.

A key finding from these previous studies is the importance of accounting for changes in thermal and transport properties to accurately predict burning rate, flame stand-off and flame temperature. The objective of the present study is to devise a hydrocarbon droplet model that allows for a general description of property variation, yet is computationally efficient so it may be used in larger scale spray simulations. The approach is based on a newly developed multizone, semi-analytical approach where local convection-diffusion solutions are used to describe the variation of temperature and composition (species mass fractions) within each zone. Analytical results are derived to determine the flame temperature and stand-off ratio in the context of a flame-sheet approximation which allows for the use of an adaptive, flame-fitted zone "mesh". The solution algorithm for the resulting eigenvalue problem is straight-forward, requiring no matrix inversion and therefore is computationally efficient. The multizone description can be adjusted to the limit of a two-zone model where accurate local estimates of burn rates are not required.

This study starts with the formulation of the quiescent quasi-steady multizone model in chapter 2. It is broken up into four sections. The first two describe the model formulation and its implementation. The third discusses a brief sum-

mary on amending the model to account for purely evaporating droplets. The fourth section discusses the comparison with experimental data. Chapter 3 describes convective and transient extensions to the model in its first section. The second section discusses the simulation results in comparison with experimental data. The final chapter covers the conclusions drawn in this study.

Chapter 2

Quiesent Quasi-steady Burning

2.1 Model Formulation

The particle is assumed to be spherically symmetric with an infinitely thin flame sheet located at $r = r_f$ (see Figure 2.1). The single step reaction mechanism is simply $m_F + \nu_O m_O \rightarrow \sum \nu_p m_p$. Assuming the species only diffuse from concentration gradients (Fickian diffusion), the system of ordinary differential equations describing the steady-state flow in the inner and outer regions of the flow are,

$$Y_i \dot{m} - 4\pi r^2 \rho D_{i-m} \frac{dY_i}{dr} = \dot{m}_i \tag{2.1a}$$

$$\sum h_i \dot{m}_i - 4\pi r^2 k \frac{dT}{dr} = \dot{Q} \tag{2.1b}$$

where $\dot{m}_i$ is the mass flow of the i^{th} species, $\dot{m}$ is the overall mass flow-rate and $\dot{Q}$ is the overall energy flow-rate (to be defined). The diffusion coefficient D_{i-m} represents the diffusion of the i^{th} species in the mixture. Note, Eq. (2.1a) does not automatically satisfy overall mass conservation, *i.e.*, $\sum \dot{m}_i \neq \dot{m}$, which serves as a constraint for determining the diffusion coefficients. Various approximations exist for constraining D_{i-m} [34, 35]. Unfortunately, none of the analytical methods allow for each species to have its own diffusion coefficient and still satisfy overall mass conservation. The simplest approximation is to assume all species have equal diffusion coefficients in each zone. The current study assumes this to be the case. The variation in transport properties due to composition and temperature changes are accounted for by decomposing radial distribution of properties into an arbitrary number of zones, as shown in Figure 2.1. Zones 1 through f reside in the inner region, between the droplet surface and the flame. Zones $f+1$ through ∞ reside in the outer region, between the flame and the far-field. The outer and inner boundaries of each zone, or shells, are defined as r_k and r_{k-1} where k is the zone number. At the droplet surface, $k = 0 \equiv s$ (*i.e.*, $r_0 = r_s$). For the inner region, $s < k \leq f$ and $D_{i-m} = D_{F-m}$, where D_{F-m} is the diffusivity of the fuel into the rest of the mixture. For the outer region, $f < k < \infty$ and $D_{i-m} = D_{O-m}$, where D_{O-m} is the diffusivity of the oxidizer (O_2) into the rest of the mixture.

Within each zone, the thermal and transport properties are assumed constant. The term, $\sum h_i \dot{m}_i$, in Eq. (2.1b) may be expressed as: $\dot{m} \sum \epsilon_i C_{P,i} T = \dot{m} \Lambda_P T$ where $\epsilon_i \equiv \dot{m}_i / \dot{m}$ is a mass flow-rate ratio, and $\Lambda_P = \sum \epsilon_i C_{P,i}$ is a mass flow-rate weighted specific heat. Note, Λ_P is not equal to the commonly used mass fraction weighted definition, *i.e.*, $\Lambda_P \neq C_P = \sum Y_i C_{P,i}$. For closure of the eigenvalue problem, ϵ_i is specified as a constraint for all species in the inner and outer regions. Equation (2.1a) and Eq. (2.1b) can be readily integrated to determine the composition and temperature distributions within each zone,

$$\frac{Y_{i,k-1} - \epsilon_{i,k}}{Y_{i,k} - \epsilon_{i,k}} = \exp\left[\frac{\phi}{\Gamma_{i,k}}\left(\frac{1}{r^*_{k-1}} - \frac{1}{r^*_k}\right)\right] \tag{2.2a}$$

$$\frac{\Lambda_{P,k}\, T_{k-1} - \dot{Q}_k / \dot{m}}{\Lambda_{P,k}\, T_k - \dot{Q}_k / \dot{m}} = \exp\left[\frac{\phi \Lambda_{P,k}}{k_k}\left(\frac{1}{r^*_{k-1}} - \frac{1}{r^*_k}\right)\right] \tag{2.2b}$$

where $\phi \equiv -\frac{\dot{m}}{4\pi r_s}$ is a constant, $r^* \equiv r / r_s$ is the normalized radial distance and $\Gamma_{i,k} \equiv \rho D_{i-m,k}$. The subscripts k or $k-1$ indicate shell (r, Y_i, T), zone (Γ_i, Λ_P, k), or region (ϵ_i, $\dot{Q}$) properties. Zone k is bounded by shells $k-1$ and k. From an energy balance at the fuel surface, $\dot{Q}_{in} / \dot{m} = \Lambda_{P,1} T_s - L'_{vap}$, where $L'_{vap} = L_{vap} - \dot{q}''_l / \dot{m}''$ is the effective latent heat of vaporization with $\dot{q}''_l = -k_l \, dT/dr|_{l,s}$ being the heat flux to the surface from the liquid. Neglecting heat losses from thermal radiation and finite-rate chemistry, an energy balance across the flame surface shows $\dot{Q}_{out} / \dot{m} = \dot{Q}_{in} / \dot{m} + \epsilon_{F,in} \Delta h_C = \Lambda_{P,1} T_s - L'_{vap} + \epsilon_{F,in} \Delta h_C$, where

Δh_C is the heat of combustion.

From the assumption of no product deposition into the liquid phase, the evaporating fuel is the only species with a mass flux, $\dot{m}_F = \dot{m}$. Therefore, $\epsilon_{F,in} = 1$ and $\epsilon_{i\neq F,in} = 0$. The outer region, $\epsilon_{O,out} = -\nu_O \epsilon_{F,in}$ for the oxidizer, $\epsilon_{p,out} = \epsilon_{p,in} + \nu_p \epsilon_{F,in}$ for the products of combustion, and $\epsilon_{I,out} = 0$ for the inert species.

Taking multiple ratios of Eq. (2.2a) for the fuel through the inner zones and multiple ratios for the oxidizer through the outer zones, with the condition that $Y_{F,f} = Y_{O,f} = 0$ for a total consumption of the reactants at the flame, the following relations can be derived,

$$\frac{\epsilon_{F,in} - Y_{F,s}}{\epsilon_{F,in}} = \exp\left\{\phi\left[\frac{1}{\Gamma_{F,f}}\left(\frac{1}{r^*_{f-1}} - \frac{1}{r^*_f}\right) + \sum_{k=1}^{f-1}\frac{1}{\Gamma_{F,k}}\left(\frac{1}{r^*_{k-1}} - \frac{1}{r^*_k}\right)\right]\right\} \tag{2.3a}$$

$$\frac{\epsilon_{O,out}}{\epsilon_{O,out} - Y_{O,\infty}} = \exp\left\{\phi\left[\frac{1}{\Gamma_{O,f+1}}\left(\frac{1}{r^*_f} - \frac{1}{r^*_{f+1}}\right) + \sum_{k=f+2}^{\infty}\frac{1}{\Gamma_{O,k}}\left(\frac{1}{r^*_{k-1}} - \frac{1}{r^*_k}\right)\right]\right\} \tag{2.3b}$$

Taking the ratio of these expressions and solving for r^*_f provides an expression for the flame stand-off ratio,

$$r^*_f = \frac{\frac{L}{\Gamma_{O,f+1}} + \frac{1}{\Gamma_{F,f}}}{\frac{1}{\Gamma_{F,f}}\frac{1}{r^*_{f-1}} + \sum_{k=1}^{f-1}\left(\frac{1}{\Gamma_{F,k}}\frac{1}{r^*_{k-1}} - \frac{1}{r^*_k}\right) + L\left[\frac{1}{\Gamma_{O,f+1}}\frac{1}{r^*_{f+1}} - \sum_{f+2}^{\infty}\frac{1}{\Gamma_{O,K}}\left(\frac{1}{r^*_{k-1}} - \frac{1}{r^*_k}\right)\right]} \tag{2.4}$$

where the factor $L \equiv \frac{\ln\left[\left(\epsilon_{F,in} - Y_{F,s}\right)/\epsilon_{F,in}\right]}{\ln\left[\epsilon_{O,out}/(\epsilon_{O,out} - Y_{O,\infty})\right]}$ depends only on the concentrations of

the fuel at the surface and oxidizer at the far-field.

Taking the ratio of Eq. (2.2a) to (2.2b) provides a relationship between a given species and the temperature within in a zone,

$$\frac{Y_{i,k-1} - \epsilon_{i,k}}{Y_{i,k} - \epsilon_{i,k}} = \left(\frac{\Lambda_{P,k}\, T_{k-1} - \dot{Q}_k / \dot{m}}{\Lambda_{P,k}\, T_k - \dot{Q}_k / \dot{m}} \right)^{Le_{i,k}} \tag{2.5}$$

where $Le_{i,k}$ is Lewis number for the i^{th} species in the k^{th} zone. Using the equal diffusivity species assumption to define the Lewis number, $Le_{i,k} \equiv Le_{F,k} = k_k / \left(\rho\, \Lambda_P\, D_{F-m}\right)_k$ for all species in the inner region and $Le_{i,k} \equiv Le_{O,k} = k_k / \left(\rho\, \Lambda_P\, D_{O-m}\right)_k$ for all species in the outer region. Taking multiple ratios of Eq. (2.5) through the zones in the outer region with $i = O$, the following relation is obtained,

$$\frac{\epsilon_{O,out}}{\epsilon_{O,out} + Y_{O,\infty}} = \prod_{k=f+1}^{\infty} \left(\frac{\Lambda_{P,k} T_{k-1} - \dot{Q}_{out} / \dot{m}}{\Lambda_{P,k} T_k - \dot{Q}_{out} / \dot{m}} \right)^{Le_{O,k}} \tag{2.6}$$

which is used to explicitly solve for the flame temperature,

$$T_f = \frac{1}{\Lambda_{P,f+1}} \left[\frac{\dot{Q}_{out}}{\dot{m}} + \Theta \left(\frac{\epsilon_{O,out}}{\epsilon_{O,out} - Y_{O,\infty}} \right)^{\frac{1}{Le_{O,f+1}}} \right] \tag{2.7}$$

where

$$\Theta = \left(\Lambda_{P,f+1} T_{f+1} - \frac{\dot{Q}_{out}}{\dot{m}} \right) \prod_{k=f+2}^{\infty} \left(\frac{\Lambda_{P,k} T_{k-1} - \frac{\dot{Q}_{out}}{\dot{m}}}{\Lambda_{P,k} T_k - \frac{\dot{Q}_{out}}{\dot{m}}} \right)^{\frac{Le_{O,k}}{Le_{O,k+1}}} \tag{2.8}$$

In the limit of two-zones, the properties in the inner and outer zones are equal, therefore, $\Gamma_{F,k} = \overline{\Gamma}_{F,in}$, $\Gamma_{O,k} = \overline{\Gamma}_{O,out}$, $\Lambda_{P,k} = \overline{\Lambda}_{P,in}$, $\Lambda_{P,k} = \overline{\Lambda}_{P,out}$, $Le_{F,k} = \overline{Le}_{F,in}$ and $Le_{O,k} = \overline{Le}_{O,out}$, where the $\overline{(\,)}$ notation represents an average over either the inner or outer regions. Making these substitutions, Eqs. (2.4) and (2.7) reduce to,

$$r_f^* = 1 + \frac{\overline{\Gamma}_{F,in} \ln \frac{\epsilon_{F,in} - Y_{F,s}}{\epsilon_{F,in}}}{\overline{\Gamma}_{O,out} \ln \frac{\epsilon_{O,out}}{\epsilon_{O,out} + Y_{O,\infty}}} \tag{2.9a}$$

$$T_f = \frac{T_\infty}{\left(\frac{\epsilon_{O,out}}{\epsilon_{O,out}+Y_{O,\infty}}\right)^{1/\overline{Le}_{O,out}}} + \frac{\Delta h_C - \overline{\Lambda}_{P,in}\, T_s + L'_{vap}}{\overline{\Lambda}_{P,out}} \left[1 - \frac{1}{\left(\frac{\epsilon_{O,out}}{\epsilon_{O,out}+Y_{O,\infty}}\right)^{1/\overline{Le}_{O,out}}}\right] \tag{2.9b}$$

which is the same as previous two-zone model descriptions [18, 27].

2.2 Numerical Implementation

Equations (2.2), (2.4) and (2.7), along with a relation for the fuel vapor-pressure curve, represent a coupled system of equations for the solution of Y_i, T and r_f^*. The solution of these equations employs an adaptive zone mesh that is described in terms of the number of zones in the inner region (N_{in}), bounded between $r_s^* (= 1)$ and r_f^*, and the number zones in the outer region (N_{out}), bounded between r_f^* and r_∞^*. The last shell at r_∞^* is set to an arbitrarily large number ($r_{f,two-zone}^* \times 10^{30}$) corresponding to the "far-field". The algorithm for deter-

mining the eigenvalue, $\dot{m}$, starts with the initialization of the T, Y_i and zone properties from a two-zone model estimate, in which $N_{in} = N_{out} = 1$. The number of zones needed in the inner and outer regions are first determined from the two-zone model by specifying a maximum temperature variation within a zone, ΔT_{max}. $\Delta T_{max} \geq |T_k - T_{k-1}| = \Delta T$ when the two-zone model is divided up into N_{in} inner zones and N_{out} outer zones and ΔT is constant in each region. An adaptive zone mesh is used to position the shells. In this approach, a normalized radial distance, r^{**}, is mapped to a regularized temperature-space, η. In the inner region, $r^{**}_{in} = (r^* - r^*_s)/(r^*_f - r^*_s)$ and $\eta_{in} = (T - T_s)/(T_f - T_s)$. In the outer region, $r^{**}_{out} = (r^* - r^*_f)/(r^*_\infty - r^*_f)$ and $\eta_{out} = (T_f - T)/(T_f - T_\infty)$. The motivation for mapping with respect to r^{**} instead of r^* is because r^* is a strong function of r^*_f (in η-space) but r^{**} is not. r^{**} only needs to be calculated once. Shell locations are defined in η-space as $\eta_k = k\Delta\eta$, where k is the shell number and $\Delta\eta = 1/N$. The position of r^{**}_k is determined by substituting the definitions of r^{**} and η into Eq. (2.2b) and using the properties of the two-zone estimate, resulting in the following expressions for the inner zones,

$$r^{**}_{in,k} = \frac{\left\{1/r^*_f + \frac{\bar{k}_{in}}{\phi\overline{\Lambda}_{P,in}} \ln\left[\frac{\overline{\Lambda}_{P,in}\left[\eta_{in,k}\left(T_f - T_s\right) + T_s\right] - \frac{\dot{Q}}{\dot{m}}}{\overline{\Lambda}_{P,in} T_f - \frac{\dot{Q}}{\dot{m}}}\right]\right\}^{-1} - r^*_s}{r^*_f - r^*_s} \tag{2.10}$$

and for the outer zones,

$$r^{**}_{out,k} = \frac{\left\{1/r^*_f + \frac{\bar{k}_{out}}{\phi \overline{\Lambda}_{P,out}} \ln\left[\frac{\overline{\Lambda}_{P,out}\left[\eta_{out,k}\left(T_\infty - T_f\right) + T_f\right] - \frac{\dot{Q}}{\dot{m}}}{\overline{\Lambda}_{P,out} T_f - \frac{\dot{Q}}{\dot{m}}}\right]\right\}^{-1} - r^*_f}{r^*_\infty - r^*_f}. \tag{2.11}$$

Once r^{**} is calculated, r^* is determined using the definition of r^{**}, *i.e.*, $r^*_{in} = r^*_s + (r^*_f - r^*_s) r^{**}_{in}$. Figure 2.2 illustrates the use of the adaptive mapping showing (a) the allocation of zones in r^* space and (b) the mapping of r^{**}_{in} in terms of η_{in}. As shown in Figure 2.2(a), the shells are near the surface where the temperature gradient is higher. In the outer region, the mapping results in shells are placed near the flame.

Figure A.1 is a flow chart of the overall algorithm for solving the eigenvalue problem for a burning droplet. A three-level nested iterative method is used to solve for composition, temperature field, droplet burn rate, flame stand-off ratio and flame temperature. From outer to inner, the loops are the $Y_{F,s}$-loop (Illinois algorithm [36, 37]), the properties-loop (Jacobi iteration) and the r^*_f-loop (Illinois algorithm). The initial state of the $Y_{F,s}$-loop, properties-loop and r^*_f-loop are supplied by the solution of the two-zone model (*i.e.*, $Y_{F,s}$, r^*_f and the properties) and r^* calculated from the adaptive mesh. The surface temperature is computed from vapor pressure relations given by Ewing [38] for *n*-heptane and Antoine [39] for ethanol and methanol (coefficients from NIST [40]). As indicated by Eq. (2.4), the flame stand-off, r^*_f, is a weighted sum of the the properties and

locations of the remaining zones. The zone locations, r_k^*, in-turn, depend on the flame stand-off ratio, therefore iteration is required using Eq. (2.4) to compute r_f^*. Once the r_f^*-loop has converged, the mass flow-rate, $\dot{m}$, may be determined by using either Eq. (2.3a) or Eq. (2.3b) to provide a value for $\dot{m}$.

$$\dot{m} = \begin{cases} 4\pi r_s \overline{\Gamma}_F \ln\left[\frac{\epsilon_{F,in}}{\epsilon_{F,s}-Y_{F,s}}\right] \\ 4\pi r_s \overline{\Gamma}_O \ln\left[\frac{\epsilon_{O,out}-Y_{O,\infty}}{\epsilon_{O,out}}\right] \end{cases} \tag{2.12}$$

where,

$$\overline{\Gamma}_F = \left[\sum_{k=1}^{f} \frac{1}{\Gamma_{F,k}}\left(\frac{1}{r_{k-1}^*} - \frac{1}{r_k^*}\right)\right]^{-1} \tag{2.13a}$$

$$\overline{\Gamma}_O = \left[\sum_{k=f+1}^{\infty} \frac{1}{\Gamma_{O,k}}\left(\frac{1}{r_{k-1}^*} - \frac{1}{r_k^*}\right)\right]^{-1} \tag{2.13b}$$

For temperature, T_f is first determined using Eq. (2.7). The temperature field is decoded using Eq. (2.2b), sweeping from r_f^* to both r_s^* and r_∞^*. The species are decoded using Eq. (2.2a), sweeping from r_f^* to r_s^* and r_∞^* for $i = F$ and $i = O$, respectively. The remaining species are swept from r_∞^* to r_s^*.

Once the revised temperature and species distributions are known, the mixture weighted thermal and transport properties are updated using a tabulated database. The database is constructed *a priori* using the Cantera software [41].

Species properties (*i.e.*, C_P, k, D_{i-j}, *etc.*), are tabulated for each temperature and pressure between: 300 K and 3000 K; and 0.5 ATM and 30 ATM. XML formatted tables are created by reading CHEMKIN formatted mechanism files with thermal and transport data. The *n*-heptane data are provided by the Combustion Research Group at the University of California, San Diego [42]. The ethanol and methanol data come from Lawrence Livermore National Laboratory [43]. The size of the tables are dynamically sized such that interpolation errors are less than 0.1% over the entire range of temperature and pressure. Ideal gas mixture rules are used to compute thermal properties. Mixing rules of Mathur *et al.* [44] and Bird *et al.* [45] are used to determine bulk diffusion and thermal conductivity properties.

Using the updated properties, r_f^* and r^* must be calculated again using the r_f^*-loop. The property-loop is iterated until r^* is no longer changing. The error is determined using an ℓ^2-norm of r^* between the most recently calculated values and the values from the beginning of the most recent property-loop iteration.

Lastly, a revised value of $Y_{F,s}$ is determined using Eq. (2.5),

$$Y_{F,s} = \epsilon_{F,in}\left[1 - \prod_{k=1}^{f}\left(\frac{\Lambda_{P,k}T_{k-1} - \dot{Q}_{in}/\dot{m}}{\Lambda_{P,k}T_k - \dot{Q}_{in}/\dot{m}}\right)^{Le_{F,k}}\right] \tag{2.14}$$

which is compared to the initial guess of $Y_{F,s}$ and iterated until a error tolerance of 1×10^{-8} is satisfied. Further step-by-step details on the iterative solution procedure are summarized in Appendix A.

2.3 Evaporating Droplet

It may be necessary to calculate the evaporation rate of the fuel when the droplet is simply evaporating. To extend the multizone burning model to an evaporative model, the outer region is bypassed by setting the number of zones in the outer region to zero. The inner region is therefore bounded by the surface of the droplet and the far-field. The previously stated model can be used by defining the "flame" conditions as those of the far-field. $r_f^* \equiv r_\infty^*$, $T_f \equiv T_\infty$, and $Y_{i,f} \equiv Y_{i,\infty}$. The r_f^*-loop and Eq. (2.7) are unnecessary. $\dot{m}$ can be defined solely by the inner region definition of Eq. (2.12). The limitation of $Y_{F,f}$ and $Y_{O,f}$ are no longer in effect. Fuel can diffuse to the far-field and oxidizer can diffuse to the surface.

Convergence criteria for the property-loop must be modified since r_f^*, and therefore r^*, is no longer a function of the properties. The shells are re-mapped using Eq. (2.10) in substitution with the r_f^*-loop, r^* is calculated from r^{**}, the properties are calculated normally, and the property-loop error is determined using an ℓ^2-norm of r^{**} instead of r^*.

2.4 Results

The burning of *n*-heptane, ethanol and methanol droplets over a range of oxygen environments are explored. These fuels are selected because of the wealth of

experimental data available in the literature for burn rates (K) and flame stand-off ratio (r_f^*). For each fuel, a zone refinement study is conducted to ensure the final reported results are zone independent. Figure 2.3 shows the error in K, r_f^*, T_f as a function of ΔT_{max} and total number of zones for (a) n-heptane, (b) ethanol and (c) methanol. In general, the error in computing T_f is much less than that for r_f^* and K for the same number of zones. The reason for this behavior is that r_f^* and K depend on the gradients of Y_i and T and therefore are more sensitive to the resolution near the droplet surface in the inner region and near the flame in the outer region. For each fuel, the rate of convergence for r_f^* and K using the adaptive mesh (—□—) is much higher than using a uniform mesh (—■—). With an adaptive mesh, approximately 200, 80 and 50 zones are needed to keep the error in K under 1 % for n-heptane, ethanol and methanol, respectively, compared to the $10,000+$ zones required for the uniform mesh to achieve only 10 % accuracy. For 5 % error, approximately 40, 20 and 15 zones are needed using the adaptive mesh, which is very reasonable for use in large scale spray calculations where millions of drops are being solved for.

Also shown on Figure 2.3, on the right axis, are the relative runtimes (—○—) for each case normalized by the time to run at the $\Delta T_{max} = 0.1$ case. For each fuel, as the order of magnitude of N increases, so does the normalized time, τ, with a slope of roughly unity. The overhead time can somewhat be seen for the lower values of N as the difference between cases is slightly less than one order

of magnitude of τ.

Table 2.1 shows a comparison of the multizone model predictions to experimental data and estimates using a two-zone model (shown in parenthesis). A two-zone model consistently over-estimates burn rates and stand-off ratios when compared to experimental data. The errors in burn rates are 55%, 22% and 39% for *n*-heptane, ethanol and methanol, respectively. The multizone model error is much less: 17%, 17% and 15%. Estimates of flame stand-off are still over-estimated, but are lower in error than the two-zone model. The equal-diffusivities assumption accounts for the underestimation of burning rate and the over estimation of r_f^*. Law and Law [27] state r_f^* is a strong function of diffusion in the outer region. They suggest increasing the diffusivity in the outer region will increase burn rate, decrease stand-off ratio and increase flame temperature. Of the species in the outer region, O_2 may not be the only leading order rate-limiting species. Other estimates of diffusivity in the outer region could be explored.

Figures 2.4, 2.5 and 2.6 show flame structure for *n*-heptane, ethanol and methanol, respectively. In (a), these figures show the temperature and species mass fractions vs. r^* and (b) shows the distribution of Le, Λ_P, C_P, k and Γ as a function of r^*. As shown, a step discontinuity in Λ_P, Γ and Le are observed across the flame due to the selection of ϵ_i and D_{i-m} in the inner region verses the outer region.

Figure 2.7 shows the flame structure of *n*-heptane with simulation data from Manzello *et al.* (MCKDDH00) [1] and Puri and Libby (PL91) [2]. Manzello *et al.* use a finite rate chemistry mechanism. Puri and Libby use a single-step reaction at a flame sheet, similar to this study, but with the addition of a water-gas shift equilibrium reaction. Consequently, the temperature and concentrations of fuel and oxidizer of this study match very well with Puri and Libby. The two flame sheet studies vary from those of Manzello *et al.* because of finite-rate chemistry effects.

Figures 2.8 - 2.10 show the sensitivity of (a) K and (b) r_f^* as a function of far-field oxygen concentration for *n*-heptane, ethanol and methanol, respectively. For *n*-heptane, comparisons are made to the experimental data of Lee *et al.* (LMC98) [46], Manzello *et al.* (MCKDDH00) [1], Okajima and Kumagai (OK75) [3], and Hara and Kumagai (HK90) [4]. For ethanol, comparisons are made to experimental data of Okajima and Kumagai (OK75) [3], Hara and Kumagai (HK90) [4] and Yozgatligil *et al.* (YPCKD04) [5]. For methanol, comparisons are made to experimental data of Marchese *et al.* (MDCN96) [6], Hicks *et al.* (HNW10) [7], Yang *et al.* (YJA90) [8], Lee and Law (LL92) [9], Dietrich *et al.* (DHDNSW96) [10] and Okai *et al.* (OMATKSDW00) [11].

As $Y_{O,\infty}$ increases, K appears to increase logarithmically and r_f^* decreases exponentially. Overall, the agreement of the multizone model predictions to the data is very satisfactory with errors less than 20%. In general, model pre-

dictions appear to consistently under-predicted the burn rate and over-predict flame stand-off when compared to the data. While the remaining differences could be attributed to physical processes not accounted for in the present model (*e.g.*, soot and radiation [5, 47], dilution of fuel from water vapor [6, 9], finite-rate chemistry [25], unsteady heating [24, 26], multi-dimensional effects [48], *etc.*), it is difficult to discern these effects given the apparent wide range of reported burn rates for the same pressure, temperature and oxygen environment due to variations in experimental methods.

Figure 2.11 shows the effectiveness of the multizone model to account for properties based on composition of the gas. The oxidizer far-field concentration is kept at a constant mole fraction, X_O, of 0.21. The increasing concentration of CO_2 displaces the nitrogen in the far-field. By keeping the oxidizer concentration constant, the flame is not being starved by increasing the CO_2 concentration and the effects are purely because of the property variations. The current study matches burn rate, K, very well to the experimental data of Hicks *et al.* (HNW10) [7]. The burn rate decreases slightly with the increase in CO_2 concentration.

Table 2.1. Burning rates, stand-off ratios, flame and surface temperatures for selected fuels at selected states. The two-zone calculation is denoted by parentheses ( ).

Fuel	$Y_{O,\infty}$	$T_\infty(K)$	$K(mm^2s^{-1})$		r_f^*	$T_f(K)$	$T_s(K)$
			model	exp.			
n-Heptane	0.23	298	0.53 (0.99)	0.64 [46]	11.0 (20.0)	2247 (2286)	362.1 (366.9)
	0.23	1200	0.64 (1.24)	1.02 [49]	9.2 (18.4)	2859 (2889)	363.8 (367.8)
Ethanol	0.23	298	0.45 (0.76)	0.54 [3, 4]	6.9 (11.0)	2139 (2200)	339.6 (343.4)
Methanol	0.23	298	0.46 (0.75)	0.54 [7]	5.3 (8.2)	2062 (2139)	324.4 (328.0)

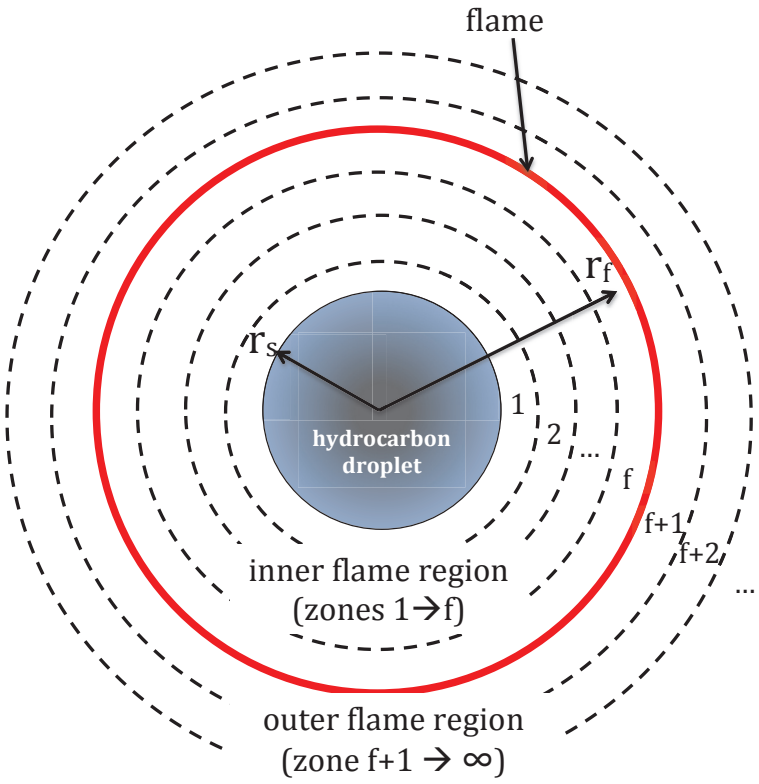

Figure 2.1. Sketch of multizone droplet description.

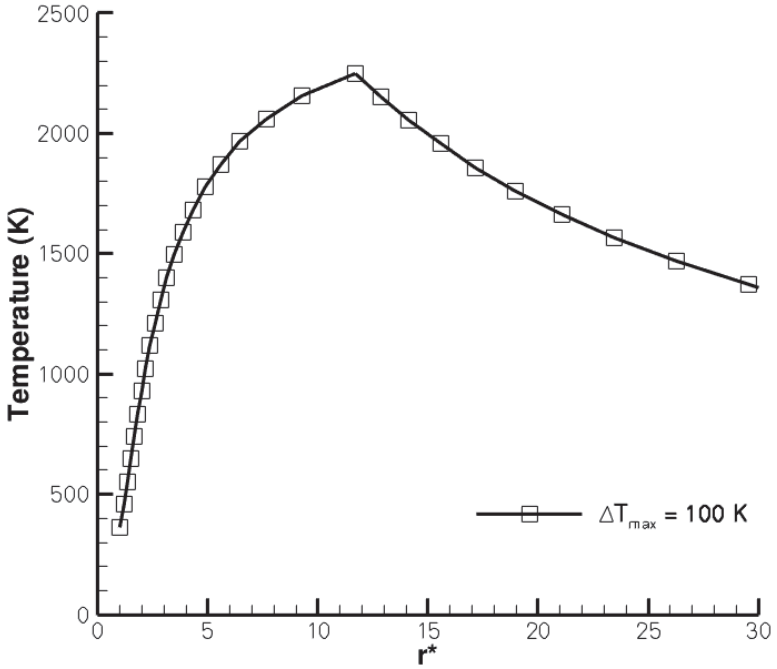

(a)

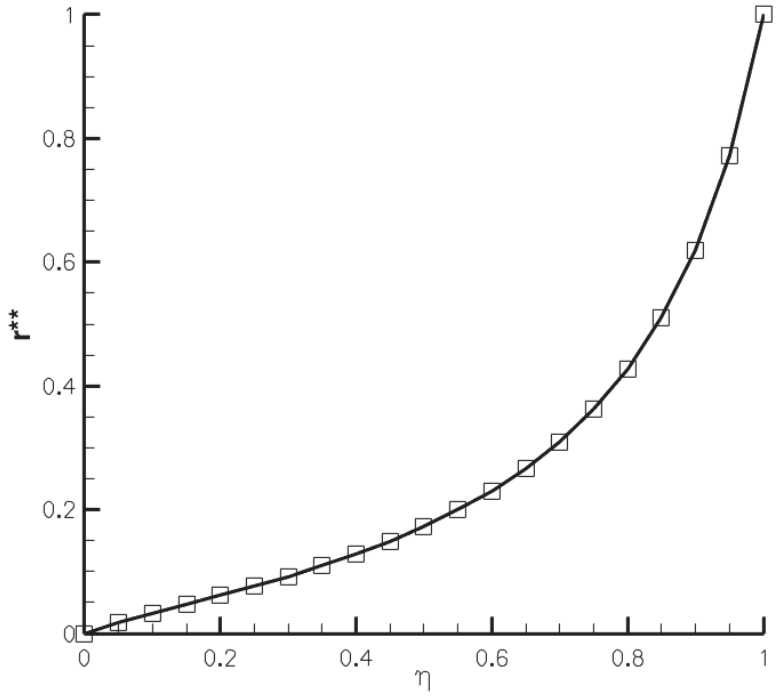

(b)

Figure 2.2. Illustration of mesh adaptivity showing (a) shell positions and (b) r_{in}^{**} verses η_{in} for $\Delta T_{max} = 100\,K$.

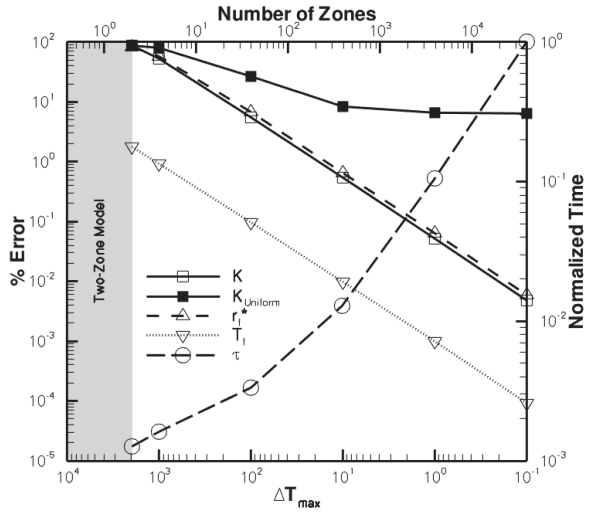

(a)

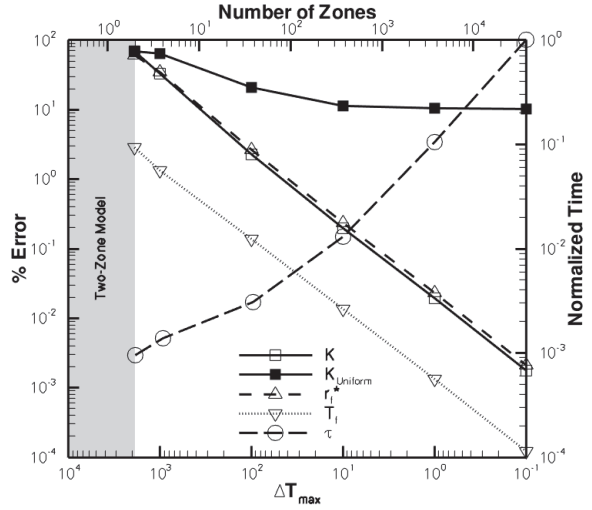

(b)

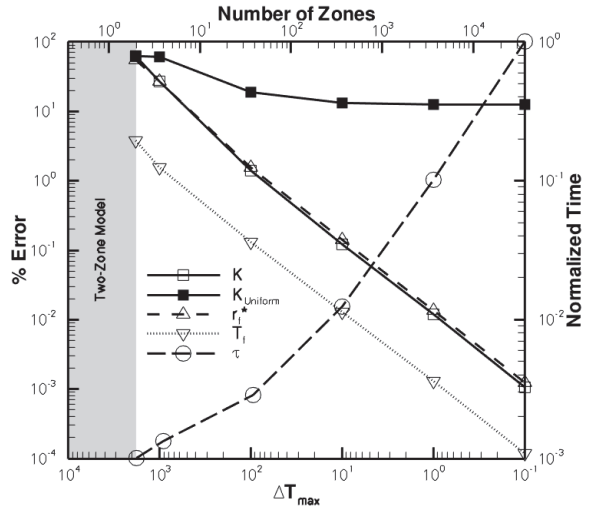

(c)

Figure 2.3. Error in K, r_f^* and T_f verses ΔT_{max} and N for (a) n-heptane, (b) ethanol and (c) methanol. For all cases $T_\infty = 298\,K$, $P_\infty = 1\,ATM$ and $Y_{O,\infty} = 0.23$.

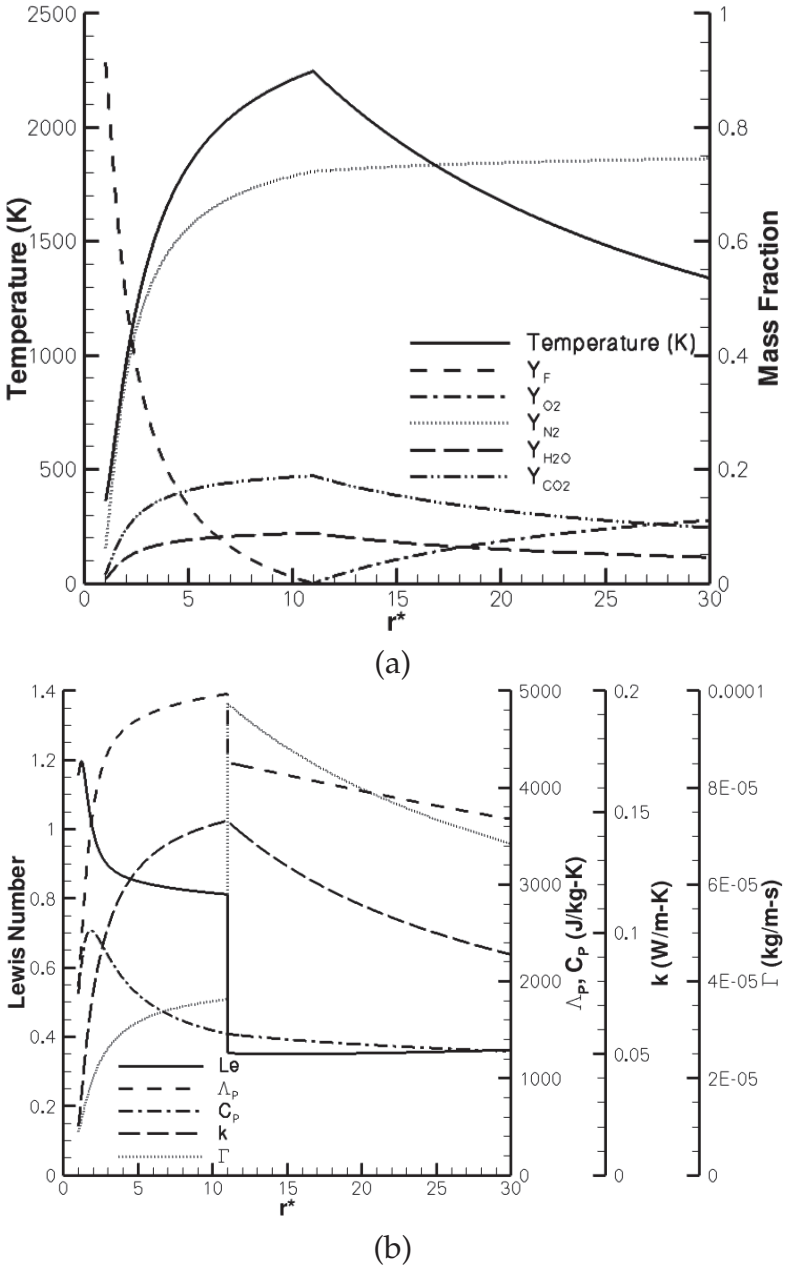

Figure 2.4. *n*-Heptane droplet flame structure showing (a) T, Y_i and (b) Le, Λ_P, C_P, k and Γ. For this case, $\Delta T_{max} = 1\,K$, $T_\infty = 298\,K$, $P_\infty = 1\,ATM$ and $Y_{O,\infty} = 0.23$.

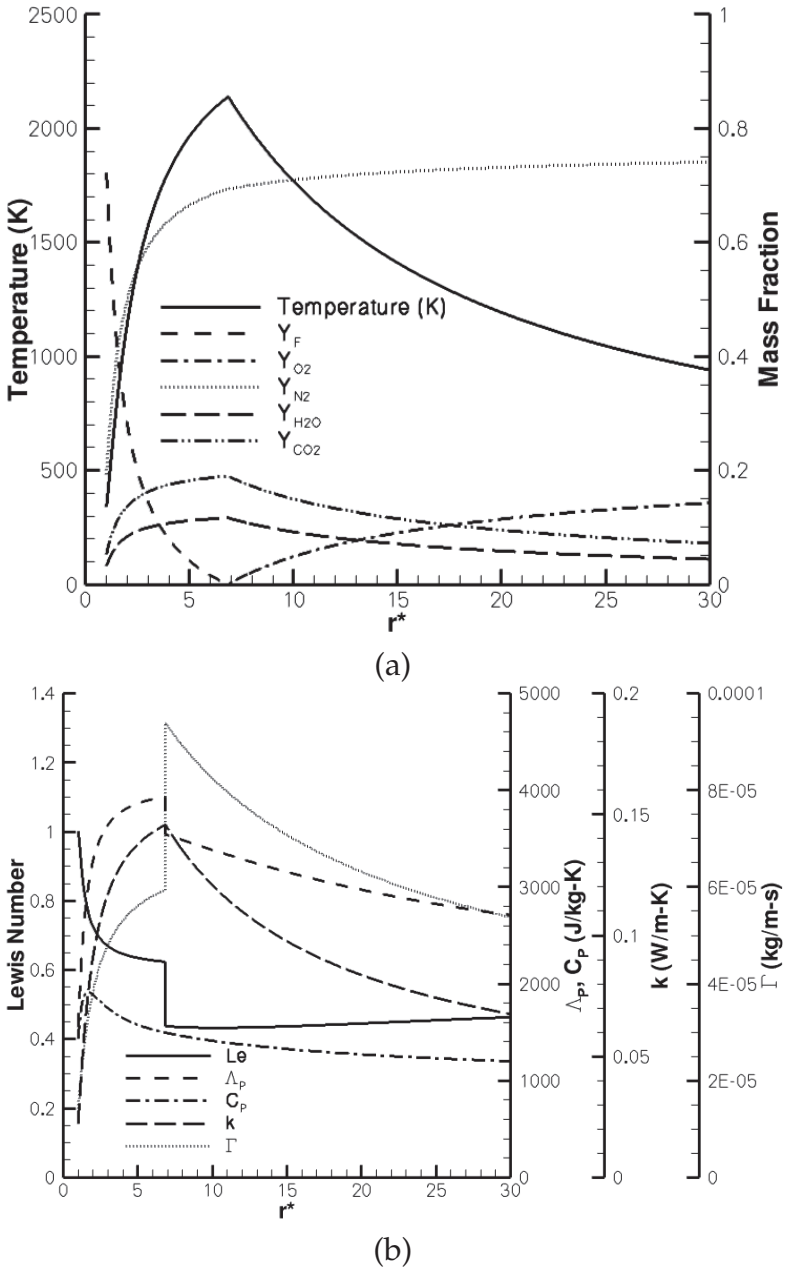

Figure 2.5. Ethanol droplet flame structure showing (a) T, Y_i and (b) Le, Λ_P, C_P, k and Γ. For this case, $\Delta T_{max} = 1\,K$, $T_\infty = 298\,K$, $P_\infty = 1\,ATM$ and $Y_{O,\infty} = 0.23$.

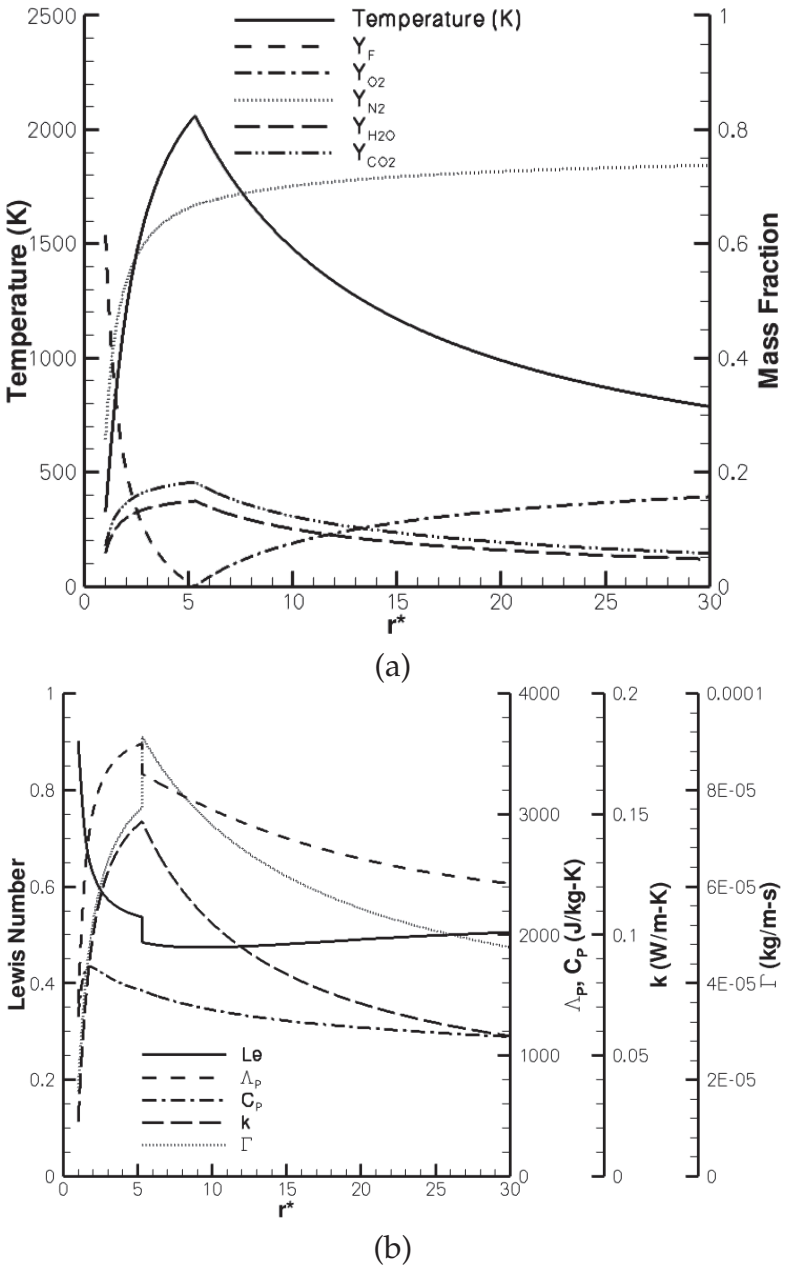

Figure 2.6. Methanol droplet flame structure showing (a) T, Y_i and (b) Le, Λ_P, C_P, k and Γ. For this case, $\Delta T_{max} = 1\,K$, $T_\infty = 298\,K$, $P_\infty = 1\,ATM$ and $Y_{O,\infty} = 0.23$.

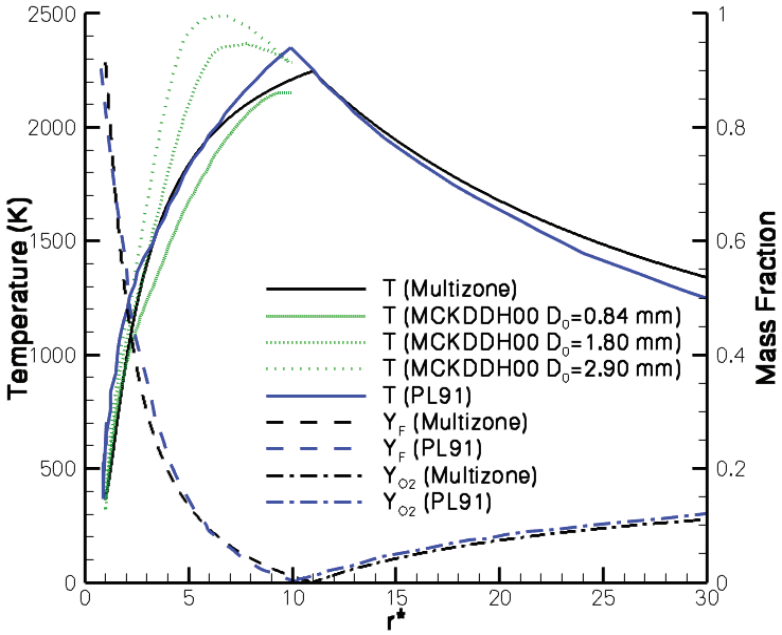

Figure 2.7. n-Heptane droplet flame structure showing T, Y_F and Y_O [1, 2]. For this case, $\Delta T_{max} = 1\,K$, $T_\infty = 298\,K$, $P_\infty = 1\,ATM$ and $Y_{O,\infty} = 0.23$.

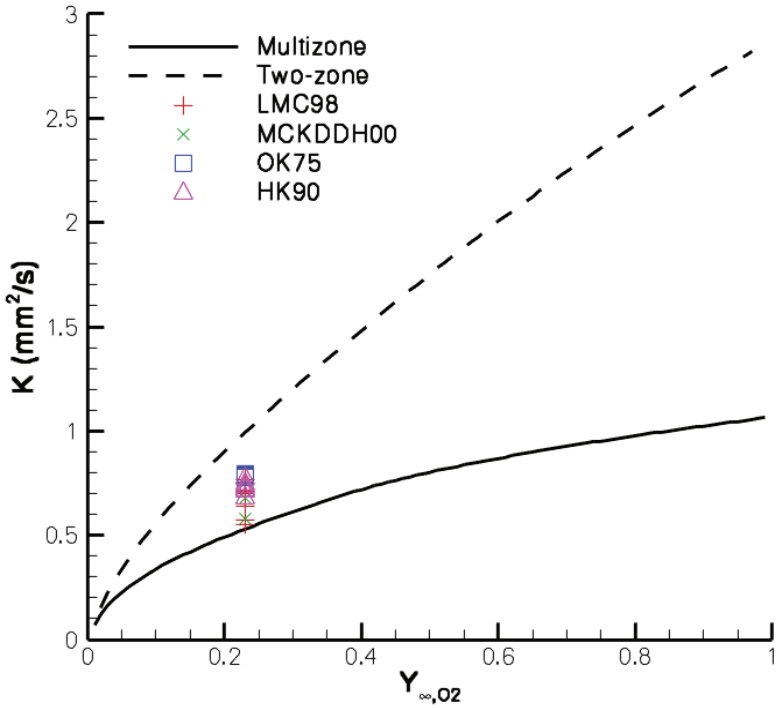

(a)

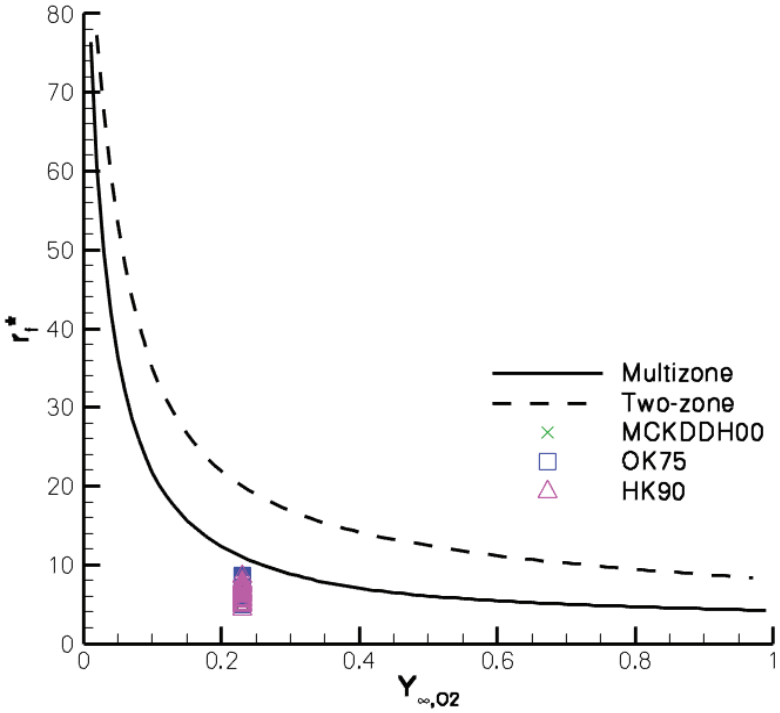

(b)

Figure 2.8. n-heptane (a) burn rate and (b) flame stand-off ratio verses $Y_{O,\infty}$ [1, 3, 4]. For all cases $\Delta T_{max} = 1\,K$, $T_\infty = 298\,K$ and $P_\infty = 1\,ATM$.

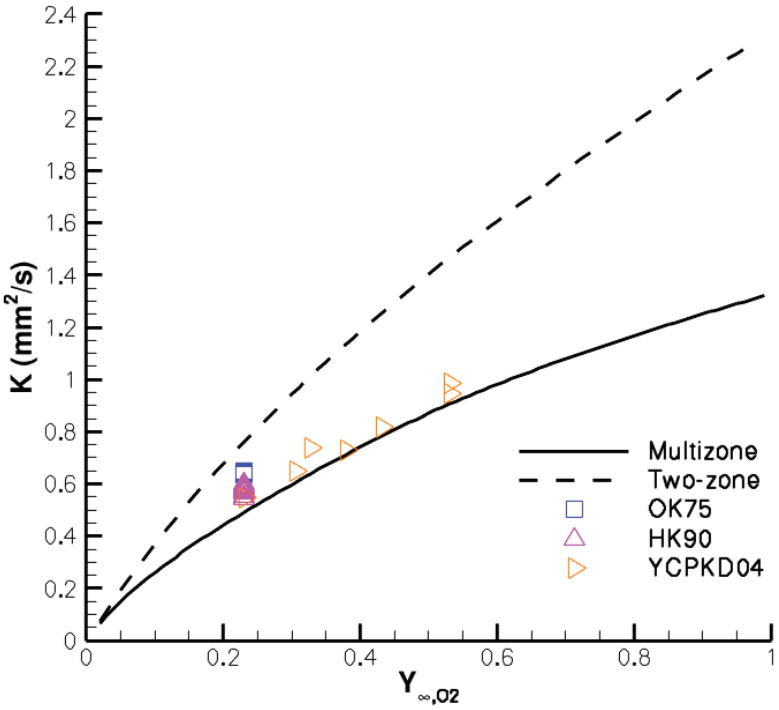

(a)

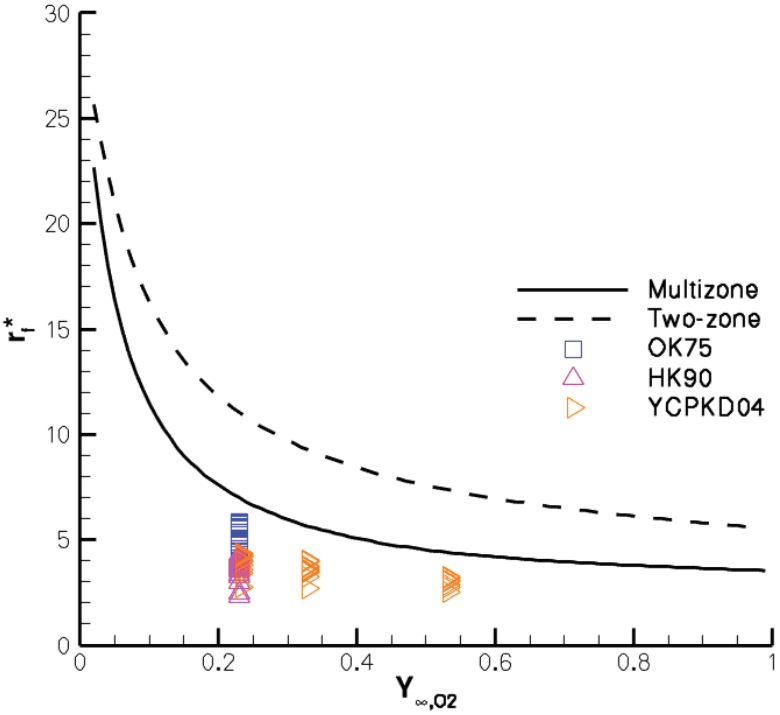

(b)

Figure 2.9. Ethanol (a) burn rate and (b) flame stand-off ratio verses $Y_{O,\infty}$ [3, 4, 5]. For all cases $\Delta T_{max} = 1\,K$, $T_\infty = 298\,K$ and $P_\infty = 1\,ATM$.

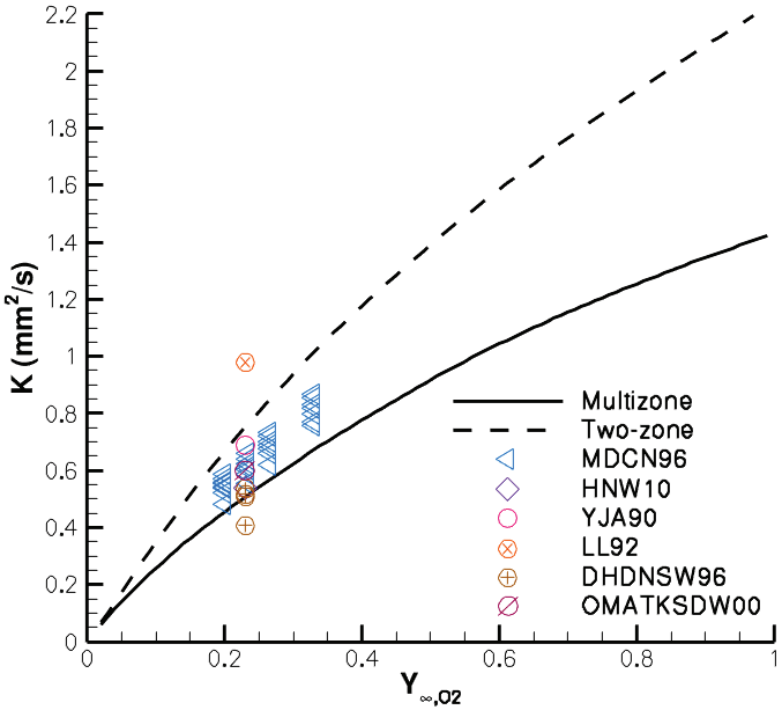

(a)

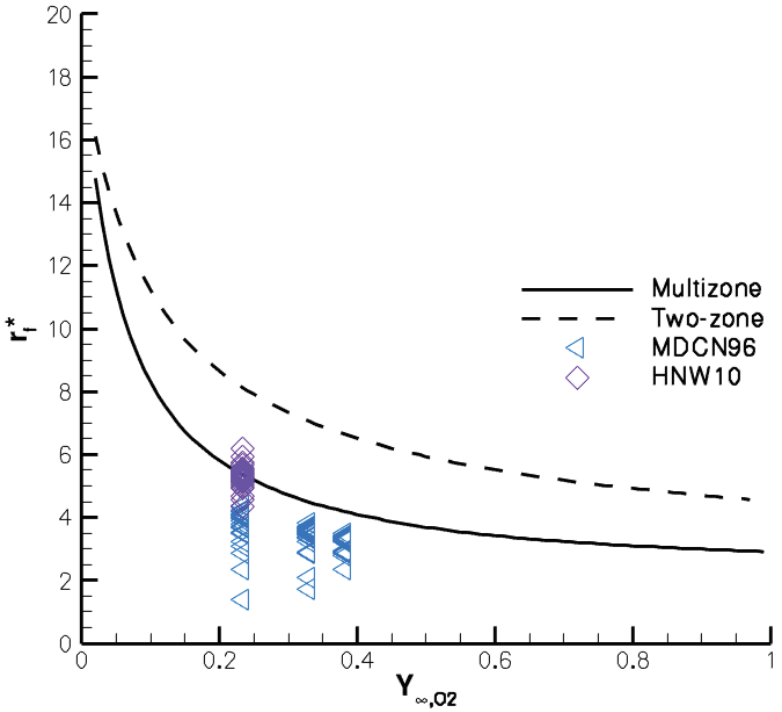

(b)

Figure 2.10. Methanol (a) burn rate and (b) flame stand-off ratio verses $Y_{O,\infty}$ [6, 7, 8, 9, 10, 11]. For all cases $\Delta T_{max} = 1\,K$, $T_\infty = 298\,K$ and $P_\infty = 1\,ATM$.

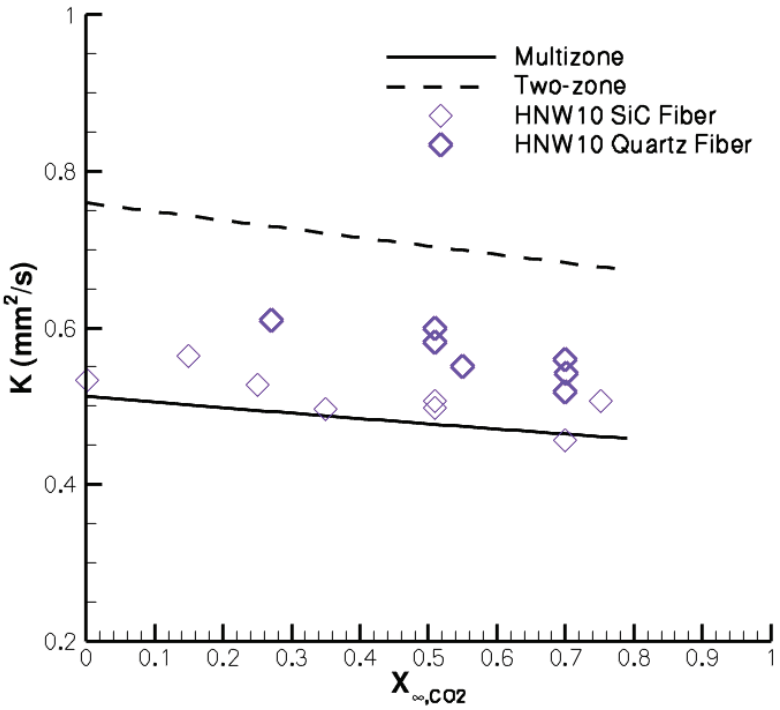

Figure 2.11. Methanol burn rate verses $X_{CO_2,\infty}$ [7]. For all cases, $\Delta T_{max} = 1\,K$, $T_\infty = 298\,K$, $P_\infty = 1\,ATM$ and $X_{O,\infty} = 0.21$.

Chapter 3

Extension to Convective Transient Burning

3.1 Formulation

The uses of a quiescent quasi-steady model for burning droplets are very limited, including matching very controlled experiments. A typical simulation will required a droplet to be moving with respect to the gases around it. The mass flow rate of fuel evaporating from the surface of the droplet is no longer solely diffusion controlled nor is heat flow rate simply conduction controlled; there is a convective transport of both mass and heat that increase the overall burn rate. The model was extended to include convective blowing over the droplet. Additionally, the mass, momentum, and energy transport rates were used to describe time-dependent source terms to allow for transient calculations of droplet

evolution of diameter, velocity, and temperature.

3.1.1 Convection Extension

In this approach, the quiescent steady-state mass flow rate described in Eq. (2.12) can be rewritten as,

$$\dot{m} = 2\pi r_s \overline{\Gamma}_F B_m Sh_0 \tag{3.1}$$

where mass transfer number $B_m \equiv \frac{Y_{F,s}}{\epsilon_{F,in} - Y_{F,s}}$ and quiescent Sherwood number,

$$Sh_0 \equiv \frac{2\ln\left[1 + B_m\right]}{B_m} \tag{3.2}$$

The quiescent steady-state heat flow rate can be written in two ways. The first by using the effective heat of vaporization and the second by using the quiescent Nusselt number, Nu_0,

$$\dot{Q} = \begin{cases} -\dot{m} L'_{vap} \\ 2\pi r_s \overline{k\Delta T} Nu_0 \end{cases} \tag{3.3}$$

where the quiescent Nusselt number, Nu_0, heat transfer number, B_q, and the heat scaling factor, $\overline{k\Delta T}$, have yet to be defined. By taking the products of multiple ratios of Eq. (2.2b) over both inner and outer regions, $\dot{m}$ can also be shown to be,

$$\dot{m} = 4\pi r_s \overline{\psi} \ln\left[\prod_{k=1}^{\infty}\left(\frac{\Lambda_{P,k}T_k - \frac{\dot{Q}_{in}}{\dot{m}}}{\Lambda_{P,k}T_{k-1} - \frac{\dot{Q}_{in}}{\dot{m}}}\right)\right] \tag{3.4}$$

where $\overline{\psi} \equiv \left[\sum_{k=1}^{\infty}\frac{\Lambda_{P,k}}{k_k}\left(\frac{1}{r^*_{k-1}} - \frac{1}{r^*_k}\right)\right]^{-1}$. Equating both parts of Eq. (3.3), using Eq. (3.4) for $\dot{m}$, and defining the quiescent Nusslet number, Nu_0, in terms of the heat transfer number, B_q,

$$Nu_0 \equiv \frac{2\ln\left[1+B_q\right]}{B_q} = -\frac{2L'_{vap}\overline{\psi}}{\overline{k\Delta T}}\ln\left[\prod_{k=1}^{\infty}\left(\frac{\Lambda_{P,k}T_k - \frac{\dot{Q}_{in}}{\dot{m}}}{\Lambda_{P,k}T_{k-1} - \frac{\dot{Q}_{in}}{\dot{m}}}\right)\right] \tag{3.5}$$

Both definitions of Nu_0 have a values inside and outside of the logarithm, therefore the heat transfer number can be defined in two ways,

$$B_q = -\frac{\overline{k\Delta T}}{\overline{\psi}L'_{vap}} = \prod_{k=1}^{\infty}\left(\frac{\Lambda_{P,k}T_k - \frac{\dot{Q}_{in}}{\dot{m}}}{\Lambda_{P,k}T_{k-1} - \frac{\dot{Q}_{in}}{\dot{m}}}\right) - 1 \tag{3.6}$$

The heat scaling factor can be solved for directly,

$$\overline{k\Delta T} = \overline{\psi}L'_{vap}\left[1 - \prod_{k=1}^{\infty}\left(\frac{\Lambda_{P,k}T_k - \frac{\dot{Q}_{in}}{\dot{m}}}{\Lambda_{P,k}T_{k-1} - \frac{\dot{Q}_{in}}{\dot{m}}}\right)\right] \tag{3.7}$$

Once the quiescent Sherwood and Nusselt numbers are calculated, a simple Ranz-Marshall [50] correlation is used to scale to convective Sherwood and Nusselt numbers,

$$Sh = Sh_0\left(1 + \frac{1}{3}Re^{\frac{1}{2}}Sc^{\frac{1}{3}}\right) \tag{3.8}$$

$$Nu = Nu_0 \left(1 + \frac{1}{3} Re^{\frac{1}{2}} Pr^{\frac{1}{3}}\right) \tag{3.9}$$

The convective mass and heat flow rates can be written,

$$\dot{m}_{conv} = 2\pi r_s \overline{\Gamma}_F B_m Sh \tag{3.10}$$

$$\dot{Q}_{conv} = 2\pi r_s \overline{k\Delta T} Nu \tag{3.11}$$

3.1.2 Transient Extension

The source terms for mass, momentum, and energy from the liquid phase can be defined,

$$\frac{dm_l}{dt} = -2\pi r_s \overline{\Gamma}_F B_m Sh \tag{3.12}$$

$$\frac{d\mathbf{v}_l}{dt} = \frac{3C_D \rho_\infty}{8\pi r_s \rho_l} |\mathbf{v}_\infty - \mathbf{v}_l| (\mathbf{v}_\infty - \mathbf{v}_l) + \mathbf{g} \tag{3.13}$$

$$\frac{dT_l}{dt} = -\frac{3}{2r_s^2 \rho_l C_{P,l}} \left[\overline{k\Delta T} Nu + \overline{\Gamma}_F B_m Sh L_{vap}\right] \tag{3.14}$$

For a less expensive computation, these source terms were linearized such that the mass, velocity, and temperature of the liquid phase could be explicitly

solved for,

$$m_l\left(t+\Delta t\right)=\frac{4}{3}\pi\rho_l\left[-\frac{B_m Sh\overline{\Gamma}_F}{\rho_l}\Delta t+r_s^2\left(t\right)\right]^{\frac{3}{2}} \tag{3.15}$$

$$\mathbf{v}_l\left(t+\Delta t\right)=\mathbf{g}\Delta t+\mathbf{v}_\infty-\left[\mathbf{v}_\infty-\mathbf{v}_l\left(t\right)\right]\exp\left[-\frac{3\rho_\infty C_D}{8\rho_l r_s}\left|\mathbf{v}_\infty-\mathbf{v}_l\left(t\right)\right|\Delta t\right] \tag{3.16}$$

$$T_l\left(t+\Delta t\right)=\widetilde{T}_s-\left[\widetilde{T}_s-T_l\left(t\right)\right]\exp\left[-\frac{3k_l}{\rho_l C_{P,l} r_s^2}\Delta t\right] \tag{3.17}$$

where $\widetilde{T}_s$ is an effective surface temperature,

$$\widetilde{T}_s=T_l\left(t\right)-\frac{\overline{k\Delta T}Nu+\overline{\Gamma}_F B_m Sh L_{vap}}{2k_l} \tag{3.18}$$

The accuracy of the solution is determined by the time step, $\Delta t\equiv\frac{\Delta t}{\tau}\tau$, where $\frac{\Delta t}{\tau}$ is a user-defined factor and τ is the characteristic time of the burning droplet defined as the minimum characteristic time for mass, momentum, and energy,

$$\tau=min\left\{\frac{D_0^2}{K},\frac{8\rho_l r_s}{3\rho_\infty C_D\left|\mathbf{v}_\infty-\mathbf{v}_l\right|},\frac{2\rho_l r_s^2}{3Nu\overline{\psi}}\right\} \tag{3.19}$$

where D_0 is the initial diameter of the droplet, $K=\frac{2\dot{m}}{\pi\rho_l r_s}$ is the burn-rate, and C_D is the standard coefficient of drag on a sphere.

3.2 Results

Figure 3.1 shows representative results for the time dependent change in D^2 and flame stand-off ratio, r_f^*, with comparison to experimental data from Hicks *et al.* [7]. Several cases are considered with increasing levels of CO_2 dilution. Experimentally, the dilution of CO_2 was introduced by displacing the available N_2 such that the overall mole fraction of O_2 remained constant. Since the modeling does not include finite-rate chemistry, the variation in predicted burn rates and flame stand-off is due to changes in bulk transport and thermal properties. As discussed by Hicks *et al.* [7], displacing N_2 with CO_2 reduces the thermal conductivity thereby reducing the heat transfer to the surface from the flame. A reduction in heat transfer to the surface reduces the evaporation rate and therefore the burning rate. Consistent with these observations, the multizone shows a reduction in the burning rate with increasing CO_2 due to the reduction in thermal conductivity. The simulations shown in Figure 3.1 were calculated using an ODE solver with source terms for mass, momentum, and energy defined by Eqs. (3.12), (3.13), and (3.14). In the experiment, the sudden decrease in flame stand-off is from flame extinguishment due to water dilution of the fuel from water vapor produced in the combustion reactions. Since this process is currently not included in the model, predictions show a greatly extended burn time relative to the data.

For the explicit solution, the mass, momentum, and energy profiles should

approach the ODE solution as Δt and $\frac{\Delta t}{\tau}$ approach zero. A resolution study was conducted to show this for a burning methanol droplet at various Reynolds numbers. Figure 3.2 shows the ℓ^2-norm error of the explicit time-step for mass, momentum, and energy decreases as $\frac{\Delta t}{\tau}$ does. Figures 3.3, 3.4, and 3.5 shows the time progression of D^2, velocity, and temperature over time for various Reynolds numbers and $\frac{\Delta t}{\tau}$ values. The smaller $\frac{\Delta t}{\tau}$ is, the closer the profile calculated from the explicit time-step solution resembles the ODE solution. At roughly $\frac{\Delta t}{\tau} = 0.01$, the explicit solution becomes time-step-size independent.

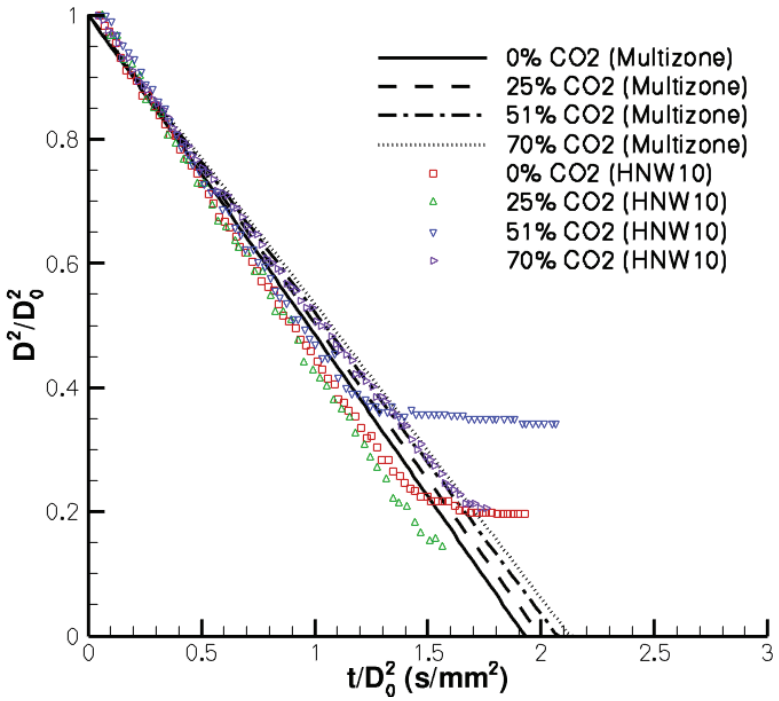

(a)

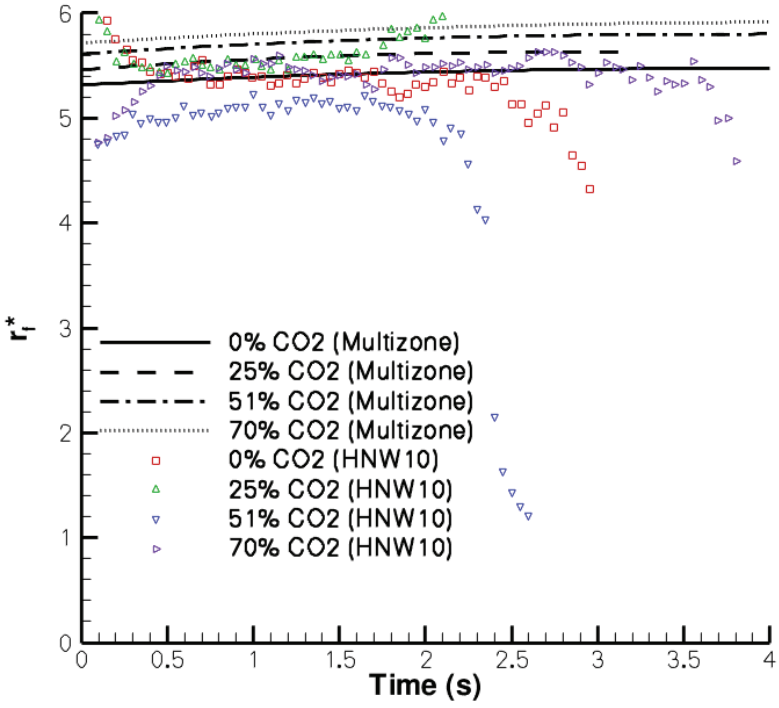

(b)

Figure 3.1. Isolated burning methanol droplet in varying CO_2 environments showing simulated and experimental (a) diameter squared vs. time normalized by the initial diameter squared and (b) stand-off ratio vs. time.

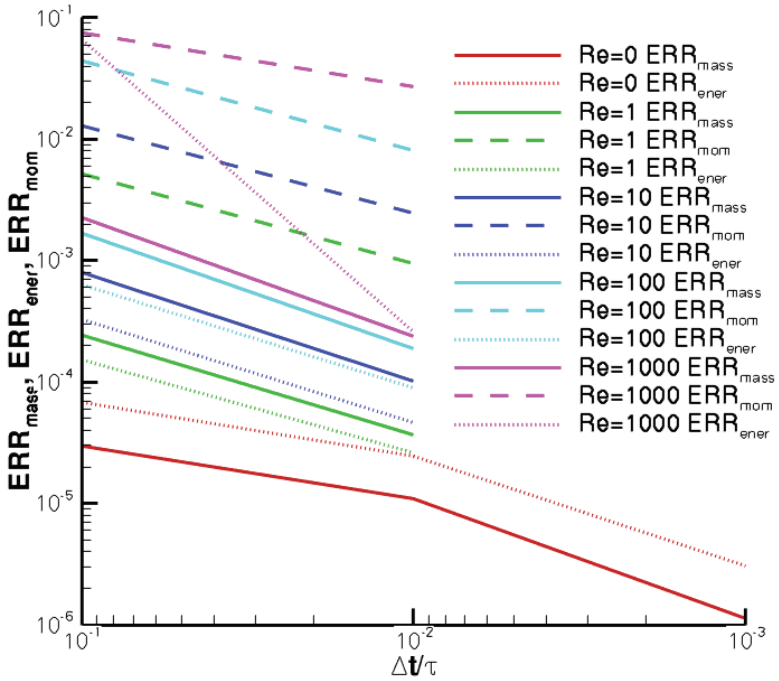

Figure 3.2. Error for mass, momentum, and energy in comparison to ODE solution through time vs. time-step size determined by the factor $\frac{\Delta t}{\tau}$ at various Reynolds numbers.

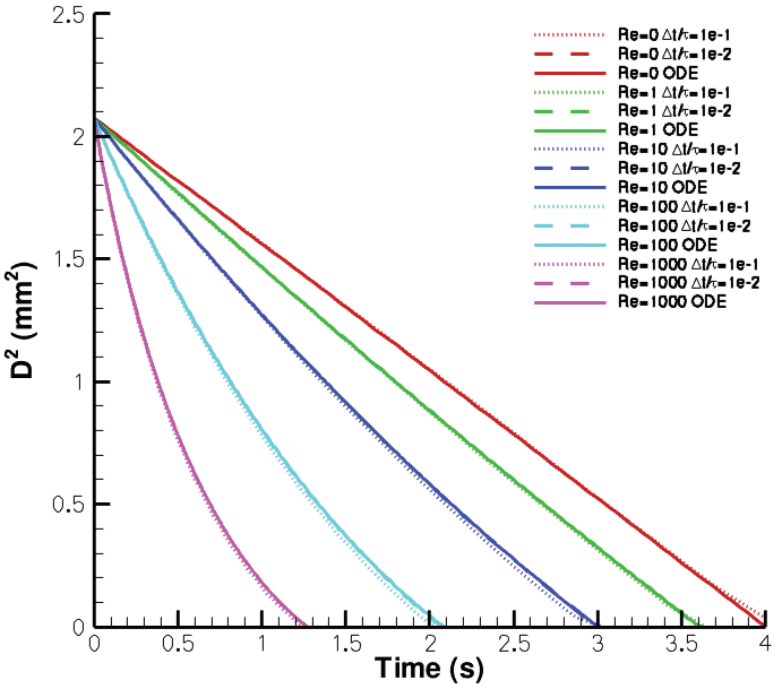

Figure 3.3. Time history for diameter squared.

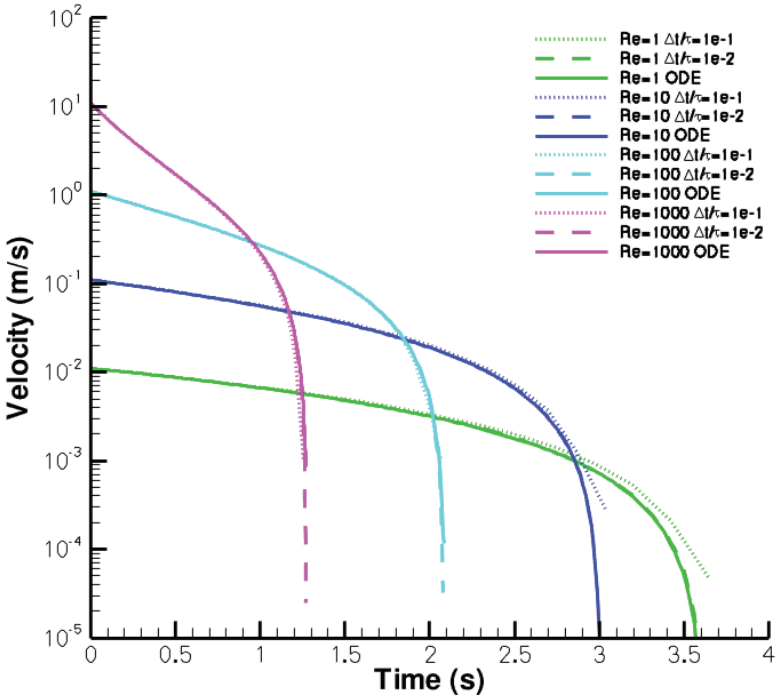

Figure 3.4. Time history for velocity.

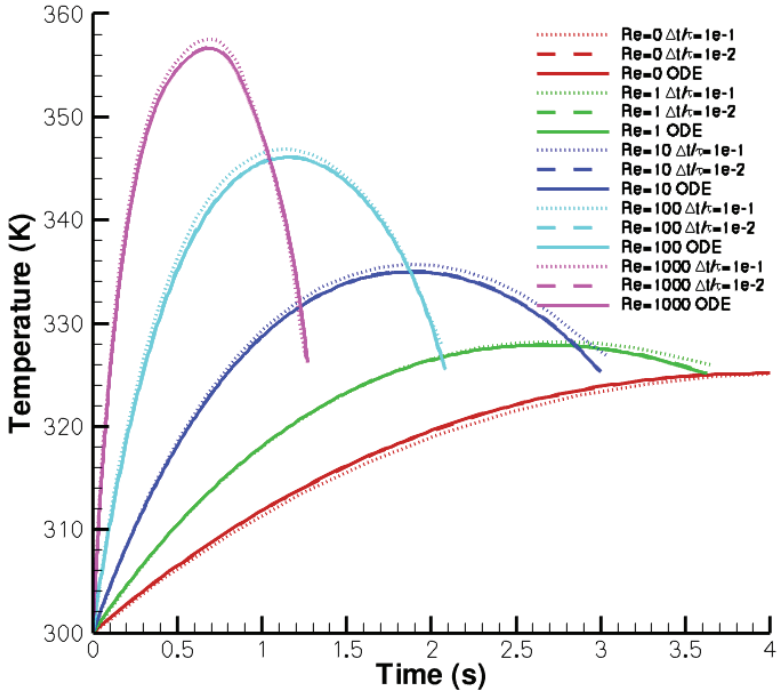

Figure 3.5. Time history for temperature.

Chapter 4

Conclusions

A multizone hydrocarbon droplet burn model is developed that accounts for variations in gas-phase thermal and transport properties. The appeal of this semi-analytical approach is a model that yields good estimates of burn rates can be determined at a fraction of the cost compared to direct numerical integration approaches, but also without incurring the errors of simplified two-zone descriptions. The use of the adaptive mesh shows excellent error convergence rates and a means to balance desired level of accuracy with computational cost. Model predictions of burn rates and flame stand-off are in favorable agreement with experimental data for the fuels and oxygen environments considered, with errors less than 20%.

Extension of the quiescent quasi-steady multizone model to a convective transient model allows implementation into an LES simulation without the need for a time dependent eigenvalue solver. Transient burning shows good com-

parison to experimental data. The transient solution was further simplified by solving explicitly for time dependent time-step independent solutions of mass, momentum, and energy while maintaining the same accuracy.

Appendix A

Solution of Eigenvalue Problem

Equations (2.2), (2.4) and (2.7), along with a relation for the fuel vapor pressure curve, represent a coupled system of equations for the solution of the radial distributions of Y_i, T and the location of r_f^*. The solution procedure for solving these equations is summarized in the following steps along with a flowchart (Fig. A.1).

1. Initialize T and Y_i at shell locations using two-zone model.
2. Solve for r^{**} using Eqs. (2.10) and (2.11).
3. Calculate r^* from r^{**}.
4. Guess a value of fuel vapor at droplet surface $Y_{F,s}$ (beginning of $Y_{F,s}$-loop).
5. Compute the partial pressure of the fuel at the surface, $P_{F,s}$, and T_s using vapor-pressure curve.
6. Guess r^*, T_k, $Y_{i,k}$, Λ_{P_k}, k_k, $\Gamma_{F,k}$, $\Gamma_{O,k}$, $Le_{F,k}$, and $Le_{O,k}$ (beginning of property-

loop).

7. Guess r^* (beginning of r_f^*-loop).

8. Solve for r_f^* using Eq. (2.4).

9. Calculate r^* from r^{**}.

10. Comparing the initially guessed value of r_f^* from step 7 to that from step 8 provides an error function that is driven towards zero using a Illinois method until an error criterion of 1×10^{-13} is satisfied (end of r_f^*-loop). Return to step 7 with new guess of r^*, if necessary.

11. Calculate $\frac{\dot{Q}_{in}}{\dot{m}}$ and $\frac{\dot{Q}_{out}}{\dot{m}}$.

12. Calculate $\dot{m}$ using Eq. (2.12).

13. Calculate T_f using Eq. (2.7).

14. Decode T using new value of T_f and Eq. (2.2b).

    a. Inner shells of T are decoded by sweeping from r_f^* to r_s^*,

$$T_{k-1} = \frac{1}{\Lambda_{P_k}} \left\{ \frac{\dot{Q}_{in}}{\dot{m}} + \left(\Lambda_{P_k} T_k - \frac{\dot{Q}_{in}}{\dot{m}} \right) \exp \left[\frac{\phi \Lambda_{P_k}}{k_k} \left(1/r_{k-1}^* - 1/r_k^* \right) \right] \right\}$$

    b. Outer shells of T are decoded by sweeping from r_f^* to r_∞^*,

$$T_k = \frac{1}{\Lambda_{P_k}} \left\{ \frac{\dot{Q}_{out}}{\dot{m}} + \left(\Lambda_{P_k} T_{k-1} - \frac{\dot{Q}_{out}}{\dot{m}} \right) \exp \left[-\frac{\phi \Lambda_{P_k}}{k_k} \left(1/r_{k-1}^* - 1/r_k^* \right) \right] \right\}$$

15. Decode Y_i fields using Eq. (2.2a).

    a. Inner shells of $Y_{F,k}$ are decoded by sweeping from r_f^* to r_s^*,

$$Y_{F,k-1} = \epsilon_{F,k} + (Y_{F,k} - \epsilon_{F,k}) \left[\frac{\phi}{\Gamma_{F,k}} \left(1/r_{k-1}^* - 1/r_k^* \right) \right]$$

    b. Outer shells of $Y_{O,k}$ are decoded by sweeping from r_f^* to r_∞^*,

$$Y_{O,k} = \epsilon_{O,k} + (Y_{O,k-1} - \epsilon_{O,k}) \left[-\frac{\phi}{\Gamma_{O,k}} \left(1/r_{k-1}^* - 1/r_k^* \right) \right]$$

    c. Outer shells of remaining species are decoded by sweeping from r_∞^* to r_f^*,

$$Y_{i,k-1} = \epsilon_{i,k} + (Y_{i,k} - \epsilon_{i,k}) \left[\frac{\phi}{\Gamma_{O,k}} \left(1/r_{k-1}^* - 1/r_k^* \right) \right]$$

    d. Inner shells of remaining species are decoded by sweeping from r_f^* to r_s^*,

$$Y_{i,k-1} = \epsilon_{i,k} + (Y_{i,k} - \epsilon_{i,k}) \left[\frac{\phi}{\Gamma_{F,k}} \left(1/r_{k-1}^* - 1/r_k^* \right) \right]$$

16. Compute mixture weighted properties of Λ_P, k, Γ_F, Γ_O, Le_F, and Le_O at each zone locations using an arithmetic average of temperature and composition from neighboring shells. Mixture weighted transport properties are determined using Cantera.

17. Compute the ℓ^2-norm error between r^* from step 6 to that from step 9. Using

a Jacobi method, iterate until an error criterion of 1×10^{-12} is satisfied (end of property-loop). Return to step 6 with new guess of r^*, if necessary.

18. Calculate $Y_{F,s}$ from Eq. (2.14).

19. Comparing the initially guessed value of $Y_{F,s}$ from step 4 to that from step 18 provides an error function that is driven towards zero using the Illinos algorithm until an error criterion of 1×10^{-8} is satisfied (end of $Y_{F,s}$-loop). Return to step 4 with new guess of $Y_{F,s}$, if necessary.

20. Calculate $\overline{\Gamma}_F$, $\overline{k\Delta T}$, Sh_0, and Nu_0 using Eqs. (2.13), (3.7), (3.2), and (3.5).

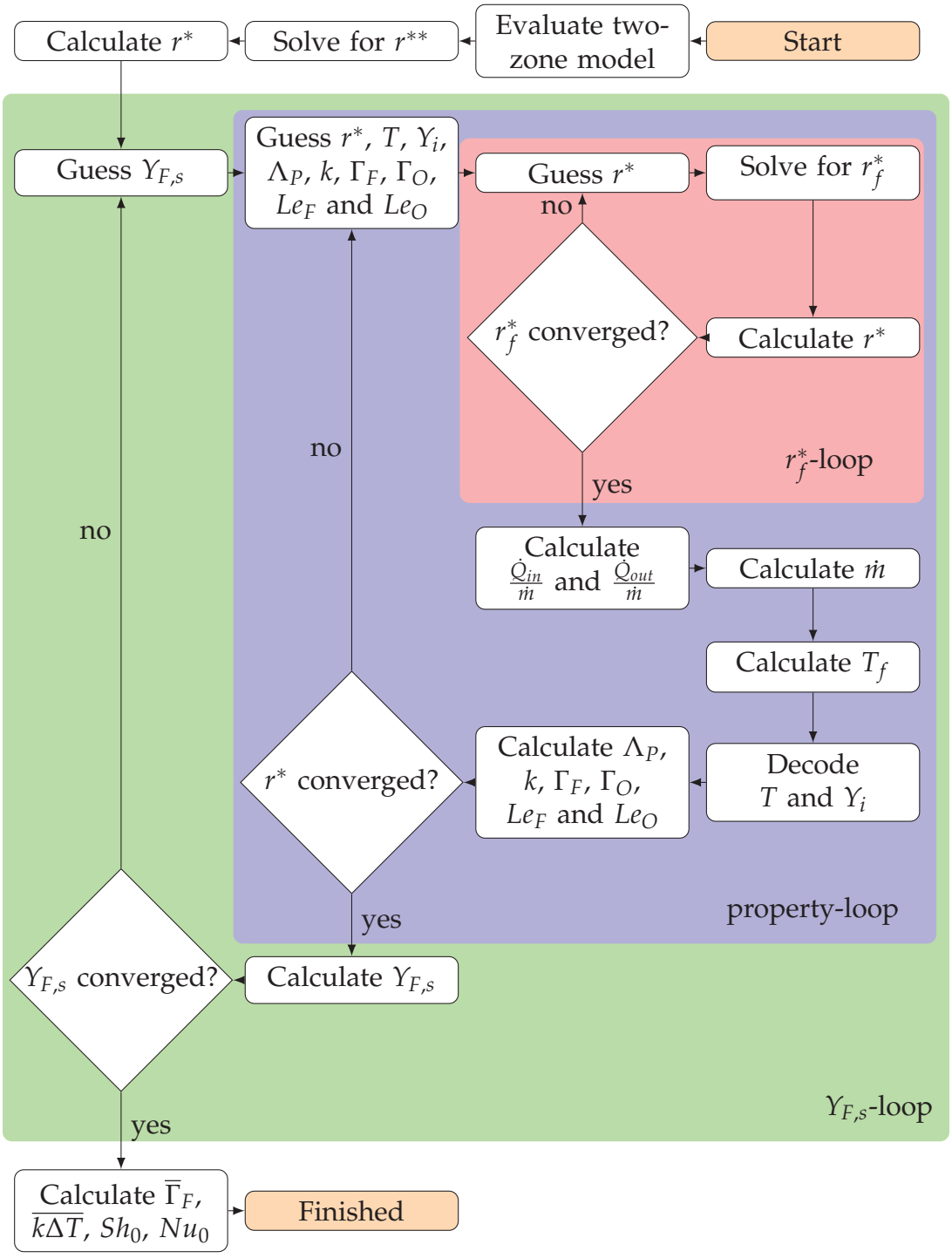

Figure A.1. Flow chart of algorithm for solution of droplet eigenvalue problem.

Bibliography

[1] S. L. Manzello, M. Y. Choi, A. Kazakov, F. L. Dryer, R. Dobashi, and T. Hirano. *Proceedings of the Combustion Institute*, 28 (2000) 1079–1086.

[2] I. K. Puri and P. A. Libby. *Combust. Sci and Tech.*, 76 (1991) 67–80.

[3] S. Okajima and S. Kumagi. *Proc. Combust. Inst.*, 28 (1975) 401–417.

[4] H. Hara and S. Kumagai. *Proc. Combust. Inst.*, 23 (1990) 1605–1610.

[5] A. Yozgatigil, S. Park, M.Y. Choi, A. Kazakov, and F.L. Dryer. *Combust. Sci. and Tech.*, 176 (2004) 275–282.

[6] A.J. Marchese, F.L. Dryer, R.O. Colantonio, and V. Nayagam. *Proc. Combust. Inst.*, 26 (1996) 1209–1217.

[7] M.C. Hicks, V. Nayagam, and F.A. Williams. *Comb. and Flame*, 157 (2010) 1439–1445.

[8] J.C. Yang, G.S. Jackson, and C.T. Avedisian. *Proc. Combust. Inst.*, 23 (1990) 1619–1625.

[9] A. Lee and C.K. Law. *Combust. Sci. Tech.*, 86 (1992) 253–265.

[10] D.L. Dietrich, J.B. Haggard Jr, F.L. Dryer, V. Nayagam, B.D. Shaw, and F.A. Williams. *Proc. Combust. Inst.*, 26 (1996) 1201–1207.

[11] K Okai, O. Moriue, M. Araki, M. Tsue, M. Kono, J. Sato, D.L. Dietrich, and F.A. Williams. *Combustion and Flame*, 121 (2000) 501–512.

[12] G. M. Faeth. *Prog. Energy Combust. Sci.*, 9 (1983) 1–76.

[13] G. M. Faeth. *Prog. Energy Combust. Sci.*, 13 (1987) 293–345.

[14] W. A Sirignano. *Prog. Energy Combust. Sci.*, 9 (1983) 291.

[15] W. A. Sirignano. *Fluid Dynamics and Transport of Droplets and Sprays*. Cambridge University Press, Cambridge, UK, 1999.

[16] F. A. Williams. *Combustion Theory*. The Benjamin/Cummings Publishing Company, Menlo Park, CA, 1985.

[17] A. Liñan and F. A. Williams. *Fundamental Aspects of Combustion*. Oxford University Press, New York, 1993.

[18] C. K. Law. *Combustion Physics*. Cambridge University Press, 2006.

[19] K. K. Kuo. *Principles of Combustion*. John Wiley and Sons, Inc., 2005.

[20] S.R. Turns. *An Introduction to Combustion*. McGraw Hill, New York, NY, 2000.

[21] I. Glassman and R. A. Yetter. *Combustion*. Academic Press, 2008.

[22] B. Spaulding. *Proc. Combust. Inst.*, 4 (1953) 847–864.

[23] G. A. E. Godsave. *Proc. Combust. Inst.*, 4 (1953) 818–830.

[24] H. Wise, J. Lorell, and B. J. Wood. *Proc. Combust. Inst.*, 5 (1955) 132–141.

[25] J. Lorell, H. Wise, and R. E. Carr. *The J. of Chem. Phys.*, 25 (1956) 325–331.

[26] C. K. Law. *Comb. and Flame*, 26 (1976) 17–22.

[27] C. K. Law and H. K. Law. *Combust. Sci. and Tech.*, 12 (1976) 207–216.

[28] C. K. Law and H. K. Law. *Combust. and Flame*, 29 (1977) 269–275.

[29] M. D. Carrara and P. E. DesJardin. *Int. J. Multiphase Flows*, 32 (2006) 365–384.

[30] M. D. Carrara and P. E. DesJardin. *Int. J. Multiphase Flows*, 34 (2008) 748–766.

[31] Y. Jin and B.D. Shaw. *Int. J. of Heat and Mass Trans.*, 53 (2010) 5782—5791.

[32] M. M. Al-Sood and M. Birouk. *International Journal of Thermal Sciences*, (2007) 779–789.

[33] M. Birouk, M. M. Al-Sood, and I. Gokalp. *Conbustion Science and Technology*, (2008) 1987–2014.

[34] M. Desilets, P. Proulix, and G. Soucy. *Int. J. of Heat and Mass Trans.*, 40 (1997) 4273–4278.

[35] A. F. Mills. *Int. J. of Heat and Mass Trans.*, 41 (1998) 1955–1968.

[36] M. Dowell and P. Jarrat. *BIT Numerics*, 11 (1971) 168–174.

[37] M. Dahlquist and A. Bjork. *Numerical Methods*. Dover Publications, 1974.

[38] M.B. Ewing and J.C. Sanchez Ochoa. *J. Chem. Eng. Data*, 50 (2005) 1543–1547.

[39] C Antoine. *Comptes Rendus des Séances de l'Académie des Sciences*, 107 (1888) 681–684, 778–780, 836–837.

[40] NIST. Nist chemistry webbook. website, National Institute of Standards and Technology, 2004.

[41] D Goodwin. Cantera: An object-oriented software toolkit for chemical kinetics, thermodynamics, and transport properties. http://code.google/com/p/cantera, 2009.

[42] UCSD. Chemical-kinetic mechanisms for combustion applications. San Diego Mechanism web page, http://web.eng.ucsd.edu/mae/groups/combustion/mechanism.html, 2002.

[43] M. N. Marinov. *International Journal of Chemical Kinetics*, 31 (1999) 183–220.

[44] S. Mathur, P.K. Tondon, and S.C. Saxena. *Molecular Physics*, 12 (1967) 569.

[45] R.B. Bird, W.E. Stewart, and E.N. Lightfoot. *Transport Phenomena*. John Wiley and Sons, 1960.

[46] K.O. Lee, S.L. Manzello, and M.Y. Choi. *Combust. Sci. Tech.*, 132 (1998) 139–156.

[47] G. Xu, M. Ikegami, S. Honma, K. Ikeda, D. L. Dietrich, and P. M. Struk. *International Journal of Heat and Mass Transfer*, 47 (2004) 5807–5821.

[48] R. Maly, P. Stapf, and H. A. Dwyer. *Combustion and Flame*, 121 (2000) 181–194.

[49] C. H. Wang, X. Q. Liu, and C. K. Law. *Comb. and Flame*, 56 (1984) 175–197.

[50] W. E. Ranz and W. R. Marshall. *Chem. Engrg. Prog.*, 48 (1952) 141–173.